IN-07-TM
185253
P-92

An Experimental Investigation
of Mixing Enhancement
in a Simulated Scramjet Combustor
By Use of Swirling Jets

by

Donna Karen Kraus

B.S. Aerospace Engineering May 1991, University of Missouri-Rolla

A Thesis submitted to

The Faculty of

The School of Engineering and Applied Science
of The George Washington University in partial satisfaction
of the requirements for the degree of Master of Science

August 1993

Thesis directed by

Dr. Andrew D. Cutler
Assistant Professor of Engineering and Applied Science

Research was conducted at NASA Langley Research Center

Abstract

It is desired to maintain supersonic flow through the combustor of supersonic airbreathing engines to reduce static temperatures and total pressure losses inherent in reducing flow to subsonic speeds. Due to the supersonic speeds through the combustor, mixing of the fuel and air must by rapid for complete combustion to occur within a reasonable streamwise distance. It has been proposed that the addition of swirl to the fuel jet prior to injection might enhance the mixing of the fuel with the air. In this study the effects of swirl on the mixing of a 30° wall jet into a Mach 2 flow were experimentally investigated. Swirl was introduced into the fuel stream by tangential injection into a cylindrical swirl chamber. The flow was then accelerated through a convergent-divergent nozzle with an area ratio of two, and supersonically injected into the Mach 2 flow such that the static pressure of the fuel matched the effective back pressure of the main flow. Two different cases with swirl and one without swirl were investigated, with both helium and air simulating the fuel. Rayleigh scattering was used to visualize the flow and seeding the fuel with water allowed it to be traced through the main flow. Using histograms of the pure molecular Rayleigh scattering images, the helium concentration in the jet-mixing region of the flow was monitored and found to decrease slightly with swirl, indicating better mixing. Thresholding the water-seeded images allowed the jet-mixing region to be isolated and showed a slight increase in this area with swirl. Penetration, however, was slightly less with swirl. Rescaling the data for equal mass flow rates allowed comparison for a scramjet application of a combustor with a single injector and the desire to fuel to a specified fuel-to-oxidant ratio. These results showed a substantial increase in the spreading area with swirl, an increase in the mixing occurring in this area, and slightly better penetration.

i

Acknowledgement

There are many people who I would like to acknowledge for their assistance in this research. Foremost is my advisor, Dr. Andrew D. Cutler. I am grateful for the guidance, knowledge, and assistance he provided in performing this research. I am also grateful to Clinton J. Reese for his aide in the operations and upkeep of "the Swirljet." I would also like to acknowledge Willis Simmons, who provided me with endless knowledge in the design and operation of the experimental setup. Thanks also to Kim Benton and all the technicians of HPB who assisted in swirljet operations, and to Roger Jones for help in the drawing of the experimental setup figures for this paper.

I would like to acknowledge all of the people of the Experimental Methods Branch, especially Dr. G. Burton Northam for funding the research, Dr. Dean R. Eklund, my officemate, for his knowledge and support, and the soon-to-be-Dr. Scott E. Stouffer for his encouragement and support throughout the project.

A special thanks goes to Dr. David W. Riggins, who has served as my mentor for many years, and, from many miles away, has provided encouragement and support throughout this research.

I am grateful to my family and friends for providing support throughout the past two years. Their love and encouragement provided me the ability to successfully complete this research. A special "thank you" is extended to Christopher D. Sontag, who supported, encouraged, inspired and loved me through it all. To him, I dedicate this thesis.

Table of Contents

iv

Nomenclature

a	speed of sound
A	area
d	nozzle diameter
d_{eff}.	effective nozzle diameter
D	diameter of laser beam at lens
f	focal length
h	height of light sheet imaged on one pixel
L	height of field of view
$\dot{m}$	mass flow rate
M	Mach number
M_c	convective Mach number
n	number of moles or gas refractive index
$\dot{n}$	molar rate
n_p	mean number of particles
N	number density of air molecules
N_a	Avogadro's number
N_d	number density of particles with diameter d
p	pressure
P	number of pixels in field of view
$\bar{R}$	universal gas constant
S	ratio of water particulate scattering to air molecular scattering
sn	signal-to-noise ratio
t	thickness of light sheet

u	axial velocity
u_c	convective velocity
v_θ	tangential velocity
$2w_o$	beam waist diameter
x	distance in axial direction
z	distance normal to fuel wall
ρ	density
λ	wavelength
δ'	growth rate of shear layer
σ	Rayleigh scattering cross-section
Ω	solid angle
X	mole fraction

Subscripts

e	nozzle exit
i	incompressible
j	fuel jet
o	stagnation
p	particle
STP	standard temperature and pressure
t	throat
∞	freestream
1	high-speed stream
2	low-speed stream

1.0 Introduction

One of the current goals of the aeronautical industry is to create a single-stage-to-orbit aircraft, which would be the successor to the space shuttle. It would be able to fly at hypersonic speeds for a sustained period of time. A supersonic combustion ramjet (scramjet) engine is being explored for use as the propulsion system. Current airbreathing engines used in supersonic aircraft reduce flow speeds to subsonic for combustion. This results in high static temperatures, which require advanced materials, and produces great losses in total pressure, reducing thrust. These effects are compounded at higher flight speeds. A supersonic combustion engine minimizes combustor static temperatures and pressure losses at these high flight speeds by maintaining supersonic flow in the combustor. However, with flow proceeding through the combustor at supersonic speeds, mixing of the fuel with the air must be rapid to prevent long and thus structurally heavy combustors. Mixing is rapid if fuel is injected perpendicular to the airstream but total pressure losses can be large in this configuration, thus reducing thrust. Thrust is enhanced if fuel is injected parallel to the airstream, for which mixing is poor[1]. It has been proposed that the use of swirl in the fuel jet may enhance the mixing between the jet and the main flow[2]. Increased mixing layer growth rates have been observed for swirling air jets in air,[3,4,5,6,7] and supersonic vortex breakdown has been observed downstream of a shock wave.[3,4,5,8,9] Breakdown of the swirling flow generates considerable turbulence and thus also enhances mixing. The objective of this research was to investigate, in a non-reacting experiment, the effects that swirl, in a jet injected at a low angle with respect to the airstream, has upon mixing in a scramjet-like configuration. The simulated fuel was injected as a jet from the wall into

1

a Mach 2 airstream at a 30° angle to the surface. The fuel was injected such that its static pressure matched the effective back pressure of the main flow. One advantage of this configuration is that 30° wall jets are already known to mix relatively well with a supersonic freestream and still provide a significant thrust component.[10,11] The flows generated in this manner were investigated by imaging Rayleigh scattering from a laser light sheet. It was possible to image pure molecular scattering, which is proportional to number density for a given molecular species. Also, seeding the fuel jet with water allowed the mixing of the fuel to be tracked. From results obtained for the cases with and without swirl, conclusions concerning the mixing enhancement produced by swirl were formed.

2.0 Background

Mixing enhancement has been investigated by many researchers for many years. In 1971 McClinton[10] investigated the effect of injection angle on the interaction between sonic secondary jets and a supersonic freestream. He investigated wall injectors at 30°, 45°, 60° and 90° to the flow, and found that lower injection angles increased penetration at downstream locations and provided faster mixing of the injected gas with the freestream. However, the total pressures of the two flows remained constant for all wall injector angles studied in his experiment. Since weaker shocks were created at the lower injection angles which created a lower static pressure behind the shock, these jets were more underexpanded, would could have contributed to his results. Mays, Thomas, and Schetz[12] investigated injection angles of 15° and 30° with varying expansion ratios, again with sonic jets into a supersonic freestream. They concluded that the angle of injection had little effect on penetration or the rate of mixing, but that the ratio of jet exit pressure to the effective back pressure of the main flow did, with a higher ratio resulting in greater mixing. King, Thomas, and Schetz[13] explored the use of combined tangential-normal injection at both sonic and supersonic speeds into a supersonic airflow. They found that the combination of a sonic normal injector just downstream of a supersonic tangential injector produced greater mixing than just a normal injector alone.

Research then progressed to exploring another method of mixing enhancement: swept ramp injectors. Northam, Greenberg, and Byington[14] investigated mixing enhancement in a reacting experiment with swept and unswept ramp injectors. They employed supersonic tangential injection from the base of the ramp injectors, and explored the benefits of additional sonic normal injection just downstream of the

injectors. The swept ramp created greater vorticity and thus greater mixing of the flows, however the additional normal fuel injector had no effect on increasing the combustion efficiency. The normal injection did increase the efficiency of the unswept ramp injector, however the swept ramp injector still provided greater mixing. Stouffer, Baker, Capriotti, and Northam[15] expanded upon this research by exploring the effects of compression verses expansion swept ramp injectors, finding that combustion occurred within a shorter streamwise distance with the expansion ramp injectors, although the fuel needed to be ignited in this case whereas auto-ignition occurred with the compression-ramp injectors. Riggins and McClinton[11] computationally compared swept and unswept ramp injectors with 15° and 30° wall jets. They explored both flow losses and mixing enhancement in a reacting flow by looking at the thrust potential of the flow. They found that the swept ramp performed substantially better than the unswept, and that the 30° wall jet performed equally better than the 15° wall jet. The mixing was found to be greatest for the swept ramp, although the 30° wall jet displayed a slightly higher thrust potential at the end of the combustor due to less losses. Thus the 30° wall jet was found to yield the best results.

In 1968 Swithenbank and Chigier[2] proposed that mixing could be enhanced by adding swirl to the fuel jet. They found that radial and axial pressure gradients existed which, in the case of strong swirl, resulted in reverse flow along the axis of the jet downstream of a shock wave, which characterizes vortex breakdown. This breakdown generates a region of recirculation, and thus considerable turbulence, which enhances mixing. Although their tests were performed at subsonic speeds, they inferred that similar results could be obtained for supersonic speeds. Cattafesta and Settles[9]

investigated the interaction between a shock wave and a supersonic vortex, and the resulting vortex breakdown. They used a strut-mounted swirl injector with guide vanes ahead of a convergent-divergent nozzle to produce a supersonic swirling jet. They created a shock wave by various methods, one of which was to overexpand the swirling jet. For Mach numbers ranging from 2.5-4 they found that the strength of a shock wave required to burst a supersonic streamwise vortex is inversely proportional to the vortex strength. Delery, Horowitz, Leuchter, and Solignac[8] had found the same results at Mach numbers in the range of 1-2. Naughton and Settles[6] created a supersonic swirling jet in a parallel supersonic coflow of air in the same manner as Cattafesta and Settles[9]. Although they were trying to produce axisymmetric flow to isolate the effects of the flow vorticity on mixing, the flow produced was non-axisymmetric due to strut interactions. However, they did find increased mixing layer growth rates with swirl.

Papamoschou and Roshko[1,16] correlated the growth rate of a two dimensional (in the mean) mixing layer between two flows to the convective Mach number of the high-speed flow, defined as the Mach number relative to the speed of the eddies in the mixing layer. They found that non-dimensionalizing the growth rate of the mixing layer by the growth rate of an incompressible mixing layer with the same velocity and density ratios made the growth rate independent of these velocity and density ratios, and thus dependent only on the convective Mach number of the high speed flow. They then experimentally investigated mixing layer growth rates for convective Mach numbers ranging from incompressible to 1.5, finding that mixing layer growth rates (when non-dimensionalized as described above) decreased asymptotically to a value of about 0.2 as the convective Mach number increased to about 1.

Cutler, Levey, and Kraus[3,4,5] investigated the properties of a supersonic swirling jet discharging into the atmosphere. The swirl was produced by tangential injection into a swirl chamber ahead of a convergent-divergent nozzle, a method which produced higher helix angles in the flow than the use of guide vanes, thus providing a greater potential for mixing enhancement. They obtained pressure and temperature measurements along a diameter of the jet, finding that the core of the jet had decreased total temperatures and total and static pressures. They visualized the mixing of the jet with the atmospheric air and found that the mixing layer growth rates increased substantially with swirl, and that vortex breakdown occurred behind the shock created when the jet was overexpanded.

Although the above summary does not represent a comprehensive survey of scramjet combustor research, it does show some examples of research which led to the development of the current investigation. In the current study the combustor of a scramjet engine was modelled by a constant area duct and fuel was supersonically injected into a Mach 2 freestream in the duct through a 30° wall jet. Swirl was introduced into the fuel jet by the method of Cutler, Levey, and Kraus,[3,4,5,7] and explored as a means to enhance the mixing between the fuel jet and the main flow. Comparisons were made between swirling jets and a straight jet on the bases of injection at equal exit static pressure, given the same fuel injector nozzle. By rescaling the data, approximate comparisons on the basis of equal mass flow injection were also made.

3.0 Method

3.1 Flow Facility

The experimental research presented here was conducted in the traverse jet ("swirljet") facility, located in building 1221C of NASA Langley Research Center. This facility consisted of a 16 inch diameter 3.5 feet tall high pressure plenum onto which a Mach 2 convergent-divergent nozzle was mounted. Compressed air was supplied to the plenum from a 600 psi supply line from a central compressor station. The nozzle was followed by a 10.5 inch long constant area duct (with inner dimensions of 1.52 by 3.46 inches) simulating a combustor of a scramjet engine (shown in Figures 3.1 and 3.2), which opened to the atmosphere. Simulated fuel was supersonically injected into the duct 2.75 inches downstream of the start of the duct at a 30° angle to the axis. The supersonic speed was achieved by passage through a convergent-divergent nozzle with a nominal exit to throat area ratio of two and a nominal exit diameter of 0.25 inches. The simulated fuel was injected such that its static pressure matched the effective back pressure of the main flow, defined as the pressure behind the bow shock generated by the disturbance created by the jet flow. The effective back pressure was calculated by taking 80% of the pressure on the surface of a cone with an apex half angle of 30° in a Mach 2 flow[12]. The main flow pressure was matched to atmospheric (14.7 psia), yielding an effective back pressure of 33 psia. The origin of the coordinate system was set as the center of the fuel injector. The x-direction is the streamwise direction and the z-direction is normal to the fuel injection wall (refer to Figure 3.1), with the y-direction set by the right-hand rule.

Swirl was introduced into the fuel stream by tangential injection in the

counter-clockwise direction (looking downstream along the nozzle axis) through a top-hat shaped insert into a cylindrical "swirl" chamber. The flow was then accelerated in the axial direction by passage through the axisymmetric convergent-divergent nozzle. Three inserts, shown in Figure 3.3, were used to produce swirl. The "low-swirl" insert, having more holes for injection of the fuel than the "high-swirl" insert, introduced a lower tangential velocity into the flow. Results from these two inserts were compared to those obtained from the "straight" insert, which had radially drilled holes and thus produced a jet with no swirl component. The three inserts were designed to yield the same flow characteristics as the corresponding inserts of Cutler, Levey, and Kraus[5]. This design allows the jet exit profiles given in Reference 5 to be used as initial conditions for the fuel jet in any future CFD comparisons with the current experiment.

Two simulated fuels, air and helium, were selected for this investigation. Hydrogen is the fuel of choice for scramjet engines, but for safety reasons could not be used in the flow facility. Helium was used as a substitute for hydrogen since its molecular weight (4) is closest to that of hydrogen (2), although its ratio of specific heat capacities is different (1.67 versus 1.4). Air was used since it is cheap and available in unlimited quantities and could possibly also model hydrogen. Helium was supplied from high pressure bottles which were at ambient temperature (60-75 °F) at the beginning of a test. Air was supplied from a 1000 psi supply line from the central compressor station. The stagnation temperature of the air for both the fuel jet and the main flow was in the range of 40-65 °F. The Reynold's number per foot of the main flow was 2.94×10^7, with a mass flow rate of about 8 lb/s and a molar rate of 0.28 lb-moles/s. Table 3.1 provides measured and calculated parameters of the fuel jet for both of the fuels for all swirl

	straight case		low-swirl case		high-swirl case	
	air	helium	air	helium	air	helium
measured $(p_e/p_o)_j$	0.1158	0.0985	0.0771	0.0707	0.0272	0.0240
calculated $(p_e/p_o)_j$	0.0940	0.0686	0.0646	0.0521	0.0271	0.0232
measured $(p_t/p_o)_j$	0.3545	0.3050	0.3473	0.3275	0.1542	0.1693
calculated $(p_t/p_o)_j$	0.5283	0.4871	0.4372	0.4141	0.2287	0.2184
calculated $v_{\theta,e}/u_j$	0.0	0.0	0.2580	0.2791	0.4733	0.5127
calculated u_j/u_∞	1.051	2.766	1.070	2.735	1.088	2.677
measured $\dot{m}_j$ (lb/s)	0.2023	------	0.1435	------	0.1131	------
calculated $\dot{m}_j$ (lb/s)	0.1979	0.1070	0.1550	0.0737	0.1170	0.0508
calculated $\dot{n}_j$ (lb-moles/s)	0.00683	0.02673	0.00535	0.01842	0.00404	0.01270

Table 3.1. Flow characteristics for swirl cases for both fuels

cases. The calculation method, which was the same as that described in References 3 and 4, assumed inviscid irrotational flow in the fuel jet nozzle. The ratios of exit pressure at the edge of the jet, p_e, and throat pressure, p_t, to plenum pressure, p_o, in the fuel jet nozzle are given. Facility restraints prevented matching the pressure for the high-swirl case with air fuel, thus experimental values are given for these ratios for $p_e \approx 22$ psia. The experimentally measured values for p_e/p_o are consistently higher than the calculated ones, while the measured values of p_t/p_o are consistently lower. It should be noted that the jet nozzle contour was designed by "eye" (not, for example, by the method of characteristics), thus the nozzle may not produce completely parallel flow at its exit, contributing to the discrepancies between the measured and calculated values. Viscous effects of the boundary layer, as well as in the vortex core of the swirling jets may also contribute to the discrepancies. The amount of swirl induced by the inserts is

expressed by the ratio of the tangential component of velocity at the edge of the fuel jet at the nozzle exit, $v_{\theta,e}$, to the axial component of velocity in the fuel jet, u_j (which is not a function of radial position in the inviscid calculations). The low-swirl insert produced a tangential velocity approximately 25% the axial velocity, while the high-swirl insert produced a tangential velocity approximately 50% the axial velocity. The ratio of u_j to the nominal freestream velocity, u_∞ (calculated assuming Mach 2 freestream and equal stagnation temperature in the freestream and fuel), is seen to be relatively constant as swirl is varied, although higher for the helium fuel than the air fuel cases. Calculated jet mass and molar flow rates assumed a stagnation temperature of 77 °F and an exit static pressure of 33 psia. Experimentally measured mass flow rates were obtained for air fuel through a contract with Wyle Laboratories and Dick Munns Company, with all test units traceable to the National Institute of Standards & Technology. The measurements have an uncertainty of ±5%. The actual calibration stagnation temperatures and pressures did not exactly correspond to those used in the calculations, however they were corrected to 77 °F and to the calculated stagnation pressure given an exit pressure of 33 psia. These corrected values are the ones given in the table. The measured value was slightly higher (2%) than the calculated one for the straight case and slightly lower (3-8%) for the swirling jet cases.

Since a higher total pressure is required to generate a swirling jet of given axial velocity than a straight jet of equal axial velocity, it is of interest to see if a comparable amount of mixing enhancement could be obtained simply by increasing the total pressure of a jet without swirl. Increasing jet pressure for a given nozzle contour leads to pressure mismatch at the nozzle exit, with further expansion occurring downstream. This

further expansion leads to greater shear and forms a stronger system of shocks, both of which may act to enhance mixing. As a means to compare the mixing benefits of swirl against those of increased pressure, an additional set of data was collected for the straight case with air fuel at twice matched pressure (hereafter referred to as the twice matched pressure case). Since we used the same fuel injector for both pressure cases, the mass flow rate for the twice matched pressure case was twice the mass flow rate for the matched pressure case.

3.2 Flow Visualization

Rayleigh scattering was used to visualize the flow. This technique employed a 30 Hz pulsed Nd-YAG laser with 10 ns pulses. The frequency of the laser light was doubled, providing about 25 mJ of energy per pulse at a wavelength of 266 nm. A Brewster's angle prism was used to split the ultraviolet from residual green. For collection of the data at the side-view location, described below, a quarter-wave plate was used to rotate the plane of polarization by 90°. A plano-convex cylindrical lens and a plano-convex spherical lens, as shown in Figure 3.4, were used to form the light sheet. The spherical and cylindrical lenses were on a moveable rail system which allowed the light sheet to be formed at any position. The laser beam was brought to the rail on which the optics were mounted through a periscope (two 90° turns by mirrors). Rayleigh scattering was performed using light at a wavelength of 266 nm rather than 532 nm in order to minimize interference by dust particles. Cutler and Levey[3] found that the scattering from dust particles present in the air was much greater at the longer wavelength, while the difference in absolute signal levels of the light sheet was not large,

11

thus using the shorter wavelength provided an equal ability to visualize the flow but with less interference from the dust particles.

The flow in the duct was visualized at four separate planes. The first, the side view, is a view of a plane parallel to the axis of the duct, normal to the fuel injection wall, through the centerline of the fuel injector. The other three views are of cross-sectional planes normal to the duct axis. The duct had interchangeable wall pieces that allowed its length to be altered for flow visualization access. The side view was achieved by assembling the duct to 2.5 inches in length, of the possible 10.5 inches, on three sides. The light sheet entered the duct through one of the open sides and struck the remaining wall where the fuel was injected. The field of view was 1.05 inches in x, starting at x=-0.15 inches, by 1.05 inches in z, starting at z=0. Since the main flow pressure was matched to atmospheric, any shock waves which formed at the exit of the duct at the three shorter sides were weak, hence the flow in the field of view was undisturbed by our flow visualization technique. The camera was oriented slightly more than 90° to the light sheet so that the view of the intersection of the light sheet with the fuel injection wall was completely obscured by the edge of the wall. This had the effect of hiding a small portion of the light sheet at the fuel injection wall.

The three cross-sectional views were at x=7.8, 15.8, and 23.8 jet diameters (d_j) downstream of the fuel injector. For any one of these views all four sides of the duct were assembled to the same length, with the light sheet placed 0.2 inches downstream of the exit. This was as close as the light sheet could be placed before a significant amount of light was reflected from the duct, causing glare in the camera. The camera looked down on the exit of the duct through a 90° turning mirror placed just outside of

the flow, as depicted in Figure 3.4. The field of view was 1.5 inches in y, centered around y=0, by 1.5 inches in z, starting at z=-0.1 inches. The small amount of distortion inherent in the images, due to the viewing angle, was corrected in subsequent image processing.

Rayleigh scattering is proportional to total number density of a gas when the composition of the gas is fixed. When using air fuel, Rayleigh scattering directly shows density variations since the gas composition is fixed. When using helium fuel, the local mole fraction of helium changes as the helium mixes with the air. Here, Rayleigh scattering is proportional to the number density of helium multiplied by the helium Rayleigh scattering cross-section plus the number density of air multiplied by its Rayleigh scattering cross-section. Since the Rayleigh scattering cross-section of helium is about 0.015 that of air, helium was essentially invisible in the current experiment. Thus air density, and an approximation of air mole fraction in cross-sections of the flow where overall number density did not vary too greatly, can be seen. This technique provides an invaluable diagnostic of mixing, both instantaneously (i.e. mixing in an image of a single 10 ns laser pulse) and in the average (i.e. in an image with many laser pulses).

Another method of visualizing the mixing is to seed the fuel with a small amount of water particles, which has the effect of highlighting the region of the flow with fuel in it. This was accomplished by injecting water into the fuel through a hypodermic-type needle, approximately 50 feet upstream of the model. The opening at the end of the needle was only 0.005 inches, which had the effect, when pressure was applied to the water, of spraying the water into the fuel stream. Pressure in the range of 50-100 psi greater than the fuel pressure was applied to the water from a high pressure nitrogen

bottle. A needle-valve was used to adjust the amount of water injected. A water flow rate to 0.5-1 cc/min was used, which produced about 100 parts per million of water in the fuel stream. The water evaporated into the fuel on the way to the model, and condensed in the convergent-divergent nozzle to form very small particles of ice. In a similar experiment, Fourguette[17] et al. estimated an **upper limit** on ice particle size of 350 nm on the basis of the observed light scattering levels, and by assuming all water known to be present was condensed into these particles. For our experiment the particle size was calculated to be of the order of 50 nm, as shown in Appendix A, on the basis of observed light scattering levels and the marker shot noise of the data in regions of condensation. Due to the small size of the particles, they should follow the fuel flow, and, provided they do not sublimate, should mark the fuel flow well.

The particles probably did not sublimate. The water concentration in the main flow was estimated to be in the range of 3 to 10 parts per million. Even though this concentration is low, the main flow was supersaturated with water at Mach 2. Since the flow was supersaturated, any condensation which occurred could not sublimate at Mach 2. However, any region where the Mach number was substantially reduced, as happens in the presence of shock waves, could have enough of a temperature rise to cause sublimation. Hence, in the vicinity of the fuel injection, where shock waves were present, there could have been regions where sublimation occurred. However, there was no evidence to support this occurrence in our experiment.

Images were captured and digitized in real time by a cooled CCD camera from Photometrics, Ltd., connected to a personal computer. The images were composed of 16-bit data (65536 gray levels) and were digitized at the rate of 40000 pixels per second

with a digitization noise of about 8 electrons r.m.s. (excluding the effects of facility acoustical noise, to be discussed later). The camera was mounted on a rail system that allowed it to be moved to any location to get the desired field of view. The CCD had 512x512 pixels and quantum efficiency of about 35% at 266 nm. A commercial F4.5 105 mm focal length camera lens designed for use in the ultraviolet range was used. A 20 cm focal length single element lens was placed in front of the commercial lens for the acquisition of the data at the side view. This arrangement shortened the overall focal length of the lens, allowing a small field of view to be imaged without extension tubes, and had the added advantage that the lens combination was faster, improving signal levels. Extension tubes were used in the cross-sectional views to achieve the desired field of view. The longer focal length of the lens allowed the camera and mirror to be placed outside of the flow. The laser was operated at 6 Hz (the shutter of the 30 Hz laser was open only every 5th pulse) to allow for the acquisition of instantaneous images. Software limitations prevented the triggering of the camera from the laser pulse, so the camera exposure time was set at 167 ms to insure the capture of a single laser pulse. The computer required approximately four seconds to digitize an image. A sequence of ten of these single shot images binned 2x2 (to improve signal to noise ratio) to a size of 255x255 pixels was acquired for all swirl cases with both fuels, with and without water-seeding. For the pure molecular Rayleigh scattering cases (no water-seeding) an additional image with a ten second exposure time was acquired. This image can be considered an average of sixty instantaneous images.

Image processing was completed on a workstation using PV ~ WAVE, an image processing software package by Precision Visuals, Inc. To remove unwanted background

light levels, a background image acquired with no flow and the light sheet blocked from reaching the model was subtracted from all images. To remove the effects of the nonuniformity of the light sheet, the images were flatfielded (i.e. divided) with a reference image acquired with the light sheet at the model but with no flow. For both the background and the reference images, an average image was used for the correction, and dust particles were first removed from the average reference images. The laboratory air contained a considerable number of dust particles which were highlighted by the laser light sheet and thus seen in the reference images. Since the light sheet did not change intensity level greatly from one pixel to the next in an image, any small region of considerably higher intensity value than the surrounding pixels in the average reference images was identified as a dust particle. Once identified, the bad pixel value was replaced with a value of a neighboring pixel. Dust particles typically occupied only one pixel, although occasionally they would occupy a region 2-4 pixels in size. When this occurred, the closest non-dust-particle pixel value was used for the replacement of the bad value.

The distribution of light intensity in the light sheet varied from laser shot to shot, so flatfielding an instantaneous image with a reference image averaged over many shots did not remove all the effects of the nonuniformity of the light sheet. To try to improve the flatfielding, the following procedure was implemented. A stripe (a long narrow region) across the image where the air density was believed to be uniform was identified. Since image intensity is proportional to air density, image intensity should have been uniform in this stripe where air density was uniform. To force this area to be of uniform intensity, a scale factor was applied at each point in it. Since the light sheet, along any

one ray, was constant in intensity (although different from ray to ray) in our field of view, these scale factors were applied along an entire ray in an image to completely correct for the fluctuations in the light sheet uniformity. The cross-sectional view images were also corrected for the distortion due to the camera and mirror angles, and the portion of the image known to be the wall of the model was blacked out.

Problems during acquisition of the images included radio frequency noise from the laser and acoustical noise and vibration from the facility. The latter effect was significant in the cross-sectional views due to the close placement of the camera to the flow. To minimize these effects the camera was wrapped first in aluminum foil and then in foam. The foil shielded the camera from interference from the laser, while the foam blocked acoustical interference from flow as it discharged to the laboratory. An additional foam block was added between the flow and the camera in the cross-sectional views to further reduce the acoustical noise felt by the camera. The rails that the camera was mounted on were secured with braces and weighted down with sand and weights to prevent the propagation of vibrations. However, acoustical noise effects on the images could not be completely eliminated, and greatly increased noise levels were experienced a few times during data acquisition. At these moments reinitializing the camera (turning it off and then back on) seemed to eliminate the problem.

Errors associated with the images fall into three categories: stray light levels, light sheet nonuniformity, and camera noise. Although every effort was made to eliminate stray light, it was impossible to completely eliminate. In order to obtain an estimate of stray light levels, an image was acquired which had a small portion of the light sheet through it blocked. After subtraction of the background image, intensity

levels on the order of 10% of the freestream value existed in the shadow region where zero intensity levels would be expected. This is a significant error, since for the pure molecular Rayleigh scattering images with helium fuel the intensity values in the jet-mixing region were in the range of 30-60% of the freestream value, resulting in a background error of 15-30% of the jet-mixing region values. The second source of error in the processed images was due to light-sheet nonuniformity. The method used to correct for this nonuniformity, described above, greatly reduced these errors, although the correction was not always perfect. The third source of error came from camera noise and photon arrival noise. Camera read noise, including effects of radio frequency and acoustical interference, was about 20 electrons r.m.s. A signal-to-r.m.s.-noise ratio in the range of 8-12 existed in the freestream region of the flow at typical laser sheet intensities.

3.3 Pressure Measurements

When altering the length of the duct for flow visualization purposes, it is desired that the flow not be changed in the region upstream of the end of the duct. A complex system of shocks arises from the bow shock off the fuel jet, as it reflects off the walls while moving downstream, which should remain in the same location and of the same strength for a particular case regardless of duct length. Wall pressure taps existed along the centerline of the fuel injection wall and the opposite wall at one inch increments beginning one inch downstream of the fuel injection point on the fuel wall and two inches upstream of the fuel injection point on the opposite wall. The second wall tap downstream of the fuel injection point on the fuel wall was machined in an incorrect

18

position and was actually 0.1 inches upstream of its correct location. Stainless steel tubes, with outside diameters of 0.060 inches and wall thicknesses of 0.010 inches and ground square at one end and glued into these wall taps flush with the internal surface of the duct. The other end of each tube was attached to a pressure transducer which was part of the data acquisition system connected to a personal computer. The wall pressures were monitored to verify that the shocks remained the same for a particular swirl case regardless of duct length to verify that the flow was not being disturbed by this experimental procedure.

3.4 Mixing Layer Growth

It is believed by some people[18,19] that the addition of swirl to a supersonic jet of a light weight gas, such as helium, mixing in air would not increase mixing layer growth rates as has been observed for air-in-air jets.[3,4,5,6,7] To explore this possibility, images were acquired at the side view with no flow through the main duct and the fuel injected such that its exit static pressure matched the ambient pressure of 14.7 psia. The mixing layer was visualized in the air fuel case by simply imaging the naturally occurring condensation in the mixing layer. This condensation occurred as the cold jet air mixed with the humid ambient air. In the case of helium fuel, condensation did not occur naturally and needed to be promoted by seeding the helium with water, as described in section 3.2. It was decided to seed both fuels with water to allow for equal comparisons of their mixing layers.

4.0 Results

4.1 Pressure Measurements

Wall pressure measurements were obtained on both the fuel injection wall and the opposite wall through the length of the duct for the straight and low-swirl cases with air fuel. The duct was assembled to 4.5 inches in length, corresponding to the length of the duct used for the acquisition of the first cross-sectional view images. The pressure readings were compared to those acquired with the duct assembled to 8.5 inches in length, which corresponded to the length used for the acquisition of the third cross-sectional view images. Figures 4.1 and 4.2 show the results for the straight and low-swirl cases. Although the pressure readings changed considerably from one x-location to the next due to the bow shock created by the fuel jet reflecting off the walls, the readings were consistent with each other for a particular swirl case regardless of duct length. Trends in the wall pressures were similar for both cases at all points through the duct except for the first tap location downstream of the fuel injector on the fuel injection wall. The pressure was lower at this location for the straight case than for the low-swirl case. This reduction was because the fuel jet was not spreading near the fuel wall at this location for the straight case, while it was for the low-swirl case.

4.2 Images

All images acquired were processed by the procedure described in Section 3.2. Figures 4.3-4.6 are composite views of the flow through the duct, showing average images (10 second exposure time, without water-seeding) acquired at the side view and the three cross-sectional views. The inside edges of the duct are drawn starting at the

beginning of the fuel injector, up to the location of the acquisition of the third cross-sectional view image. Part of the fuel injection wall can be seen in the cross-sectional view images, thus this part extends outside of the inner dimensions of the duct. The exit of the fuel injector is also outlined. The side-view image shows the fuel injector and bow shock, and the cross-sectional view images depict the spreading of the fuel into the freestream. The reflected bow shock can be seen in the first cross-sectional view image. The pure Rayleigh scattering images with air fuel injection into air show less detail because of the absence of composition variation which exists with helium fuel injection into air. Figure 4.3 is the composite image for the straight case with air fuel. In the side-view image the bow shock and a little of the air fuel injection can be seen. A low density region is seen in the first cross-sectional view image, which could be caused by the expansion of the freestream into the region behind the fuel jet.

The progression of mixing through the length of the duct for the three swirl cases with helium fuel can be seen in Figures 4.4-4.6. Similar views for air fuel are less informative (as can be seen by comparing Figures 4.3 and 4.4) and are not shown. For the high-swirl case with helium fuel, average images were not acquired at all locations, thus this composite is not complete. It can be seen that the fuel spreads symmetrically into the freestream in the straight case while it spreads to one side in the low-swirl and high-swirl cases. The interactions of the vortices created in the fuel jet caused this phenomena. In the straight case two counter-rotating vortices of equal strength were created in the fuel jet when it was turned by the main flow, which provided symmetrical spreading. In the swirling jet cases one of the counter-rotating vortices was of significantly greater strength than the other, and due to reacting with its image in the wall, it moved towards one side.

4.2.1 Side View

Figures 4.7 and 4.8 show the instantaneous pure molecular Rayleigh scattering images at the side view for both fuels. The main flow is from left to right with the fuel injected from the bottom wall. The bow shock can be seen emanating from the surface in front of the fuel injector. Facility restraints described earlier prevented the acquisition of any images for the high-swirl case with air fuel. The low density core of the fuel jet can be seen in the low-swirl and high-swirl cases. The expansion of the freestream into the region behind the fuel jet caused a low density region near the wall downstream of the fuel injector, which is most evident in the straight case with air fuel. Small acoustical shocks can be seen near the fuel jet region in the helium fuel images due to the high convective Mach number of the main flow air relative to the eddies ($M_{c,2} \approx 1.17$ for helium fuel versus $M_{c,2} \approx 0.30$ for air fuel; see Appendix B). Dust particles existed in the fuel lines during acquisition of the images for the high-swirl case with helium fuel which were the cause of the bright dots in the jet-mixing region of that image. Figures 4.9 and 4.10 show the equivalent images with the water-seeded fuel. Condensation is not observed in the low density core of the fuel jet in the swirling cases, but is present in the higher density periphery, due possibly to centrifugal effects on the ice particles or to the effect of density or temperature variations on the condensation dynamics. As the fuel jet turns parallel to the main flow, the interface between the condensation region and the region without condensation in the interior of the jet becomes very ragged and unsteady, indicating the formation of large-scale turbulent eddies in the jet core. This observation is possibly a form of vortex breakdown, although there was no evidence of a region of recirculation. Figure 4.11 shows a sequence of four instantaneous images

for the low-swirl case with water-seeded helium fuel. The unsteadiness of the flow is evidenced by the shot-to-shot variations in the images.

A comparison between the water-seeded air fuel and the water-seeded helium fuel images (Figures 4.9 and 4.10) shows differences in the mixing layer between the fuel jet and the duct air. The condensation/no-condensation (i.e. fuel/no-fuel) interface, seen most clearly on the upper side of the fuel jet, appears more ragged in shape with air fuel. This is probably due to the damping effect on the turbulent eddies of the high convective Mach number with helium fuel. However, calculated mixing layer growth rates are similar for the two fuels ($\delta' \approx 0.053$ for the straight case with air fuel versus $\delta' \approx 0.059$ for the straight case with helium fuel; refer to Appendix B) due to the offsetting effects of increased shear. The effect of swirl, which is to cause an increase in the mixing layer growth rates as evidenced by an increase of the size of the eddies seen at the condensation/no-condensation interface, also appears to be the same with either air fuel or helium fuel.

4.2.2 $x/d_j = 7.8$

The first cross-sectional view images were acquired at 7.8 jet diameters downstream of the fuel injector. Figure 4.12 shows the instantaneous pure molecular Rayleigh scattering images for the three swirl cases with helium fuel at this location. The images with air fuel do not show much detail and are thus omitted. The images were acquired looking upstream, thus the main flow is out of the page, the fuel is injected from the bottom wall, and the direction of swirl is clockwise. The reflected bow shock can be seen at the top of the image and small acoustical shocks around the fuel jet. The

high-swirl case image is poor due to camera noise which was not noticed at the time of acquisition. It can be seen that the fuel spreads to one side with swirl while without swirl it spreads in the center, as was previously explained. The flow was again unsteady, and the images varied greatly from shot to shot.

The instantaneous images with water-seeded air and helium fuel at this first cross-section are shown in Figures 4.13 and 4.14. Facility restraints described earlier prevented the acquisition of images for the high-swirl case with air fuel. In the straight case the effects of the two counter-rotating vortices can be seen while in the low-swirl and high-swirl cases there is one dominant vortex. Note that water droplets are present in the straight case with helium fuel due to incomplete evaporation upstream in the fuel lines of the water injected into the fuel.

4.2.3 $x/d_j = 23.8$

The same types of images as were shown for the first cross-section are shown for the third cross-section. Figure 4.15 shows the instantaneous pure Rayleigh scattering images with helium fuel at the third cross-section. Comparison with Figure 4.12 allows the increase in spreading through the length of the duct to be seen. Figure 4.16 is a sequence of four of these instantaneous pure Rayleigh scattering images for the low-swirl case with helium fuel and depicts the unsteadiness of the flow. Figures 4.17 and 4.18 show the instantaneous Rayleigh scattering images with water-seeded air and helium fuel. The difference between the two fuels has become more noticeable by this location. For all three swirl cases the helium fuel appears to spread more laterally into the flow than the air fuel. Note that the jet-mixing region of the image for the straight case with

helium fuel is not as bright as it is in the images for the other cases. This was due to the inability to control the exact amount of water in the fuel, which periodically resulted in lower amounts of water and thus lower intensity levels in some of the images.

4.2.4 Jet Pressure Twice Matched

Additional data for the straight case with air fuel was taken, but instead of injecting the fuel such that its static pressure matched the effective back pressure of the main flow, it was injected such that its static pressure was twice the effective back pressure of the main flow. These results are shown in Figures 4.19-4.21. Figures 4.19 and 4.20 show the side view instantaneous Rayleigh scattering images for air fuel with and without water-seeding. A bright region of condensation can be seen downstream of the fuel injector which is especially noticeable in the image without water-seeding. (Note that the camera was saturated with light in this region, which caused it to wrap the intensity values, thus this dark region is actually of greater intensity value than the neighboring white region.) The jet is underexpanded, thus an expansion fan forms to reduce the pressure, and it is in this region that the condensation occurs. Presumably the reduced static temperature leads to condensation of the low level of naturally occurring water vapor, or other contaminants (e.g. CO_2). Besides this region, the rest of the image appears similar to the corresponding matched pressure image. A direct comparison, however, to the corresponding matched pressure image can not be made due to the scaling effects described below.

The cross-sectional instantaneous Rayleigh scattering images with water-seeded air fuel are shown in Figure 4.21. Recall from Section 3.1 that the mass flow rate of

the fuel in the twice matched pressure case was twice that of the matched pressure case due to the fact that the same fuel injector was used for the acquisition of both sets of data. To maintain equal mass flow rates, the area of the fuel injector for the twice matched pressure case should have been decreased by a factor of two, or thus the diameter of the fuel injector by a factor of the $\sqrt{2}$. Since the fuel injector area was not changed, the data must be appropriately scaled to account for the difference in the mass flow rates. Since the diameter of the fuel injector was the square root of two larger in the twice matched pressure case than it should have been to maintain a mass flow rate equal to that of the matched pressure case, length scales can be considered to be the square root of two larger also. Thus, $x/d_j=7.8$ twice matched pressure data needs to be compared to matched pressure data at $x/d_j=5.5$ ($=7.8/\sqrt{2}$). Likewise, $x/d_j=23.8$ twice matched pressure data needs to be compared to matched pressure data at $x/d_j=16.8$. Although neither is directly possible for the data collected in this study, some comparisons can be made. The two counter-rotating vortices can be seen in the $x/d_j=7.8$ data for both the matched and twice matched pressure images. The fuel has penetrated farther into the flow in the twice pressure image at $x/d_j=23.8$ than in the matched pressure image at $x/d_j=15.8$ (which is close to the $x/d_j=16.8$ location to which it should be compared), and also seems to be spreading laterally, which was not previously occurring with the air fuel. However, since the y and z length scales must also be scaled down by $\sqrt{2}$ in the twice matched pressure images for direct comparison to the matched pressure images, it is hard to determine from just looking at the images whether any marked improvement exists for the twice matched pressure case.

4.3 Analysis

Two methods, described below, were used to compare the amount of mixing which occurred in each swirl case. A comparison of the data obtained from the averaged histograms of the pure molecular Rayleigh scattering images and a comparison of the data obtained from the averaged thresholded images of the water-seeded fuel images allowed a determination on the mixing enhancement by the addition of swirl to be made.

4.3.1 Histograms

If the gas total number density were uniform in the cross-section, then, in the pure molecular Rayleigh scattering images with helium fuel, image intensity would be proportional to mole fraction of air (or one minus mole fraction of helium). Thus, a histogram of the image would give the probability distribution of mole fraction of air in the cross-section and could be used as a method of comparison between cases. A cross-section where perfect mixing has occurred would be one where the probability distribution of mole fraction of air has a single peak. (The flow in the duct would be of uniform mole fraction of air throughout.) Where less than perfect mixing has occurred, the probability distribution would be broader, with a peak at the freestream value (100% air) and values distributed at lower air fractions. In practice, total number density was not uniform which caused a broadening of the experimental histograms. Further broadening of the histograms was also produced by camera noise (refer to Section 3.2). This broadening, however, is likely to be similar in all cases at a given cross-section, and less than that due to lack of mixing in the flow. Thus, comparisons of the experimental histograms should allow comparisons of mixing to be made in each case.

The histogram for each single-shot pure Rayleigh scattering image (without water-seeding) in a sequence of images was computed for both air and helium fuel, and then those histograms were averaged to yield an averaged histogram used for comparison. As necessary, the images were first rescaled to account for shot-to-shot variation of light-sheet intensity. An averaged histogram found in this manner is of more interest to combustion researchers than a histogram of an average image since mixing in an instantaneous sense (where air and fuel are together at a point at the same time) is what permits combustion, rather than mixing in an average sense (which can occur due to intermittency in the flow, where air is at a point at one moment and fuel at that point at another moment). Figures 4.22 and 4.23 show the averaged histograms for each case at each cross-sectional location with air and helium fuel. Since the images for the high-swirl case with helium fuel at x/d_j=7.8 experienced high camera noise, this histogram is not shown. There is no histogram for the high-swirl case with air fuel at any location due to the flow facility limitations for this case, as described earlier. Since there is no variation in flow composition in the air fuel cases, the air fuel histograms provide a reference for the effect of broadening by number density variation and camera noise for comparison with the helium fuel histograms. It is seen that these histograms (and therefore the broadening effects) are nearly symmetrical, a fact that shall be used shortly. In the helium fuel histograms the left hump signifies an area of low mole fraction of air (i.e. high mole fraction of helium) and thus corresponds to the jet-mixing region of the image. The right hump signifies an area of high mole fraction of air, which corresponds to the freestream. As the fuel mixed with the freestream, which occurred as the flow progressed downstream through the duct, a blending of the jet-mixing region and

freestream region humps of the histogram occurred.

These averaged histograms were used to monitor the mean air and helium concentrations in the jet-mixing region of the images. To be able to distinguish between the jet-mixing region and the freestream region of the histogram, the following procedure was implemented. It was assumed that the histogram of the freestream region alone was symmetrical, as was previously discussed, and that the right half of the freestream region hump of the histogram was unaffected by the helium fuel. The freestream contribution to the histogram was then obtained by reflecting the right half of the freestream region hump around its peak, and combining this reflected half with the unreflected right half. The freestream region contribution was obtained in this manner and was subtracted from the original histogram, resulting in the jet-mixing region of the histogram being isolated. The procedure is illustrated in Figure 4.24. The solid line is the original histogram, with the dotted line being the symmetrical freestream contribution, and the dashed line being the jet-mixing region contribution. The mean mole fraction of air in the jet-mixing region was then calculated by computing the mean pixel value in this region and dividing by the mean pixel value in the freestream region. The mean helium mole fraction is then one minus the mean air mole fraction. This procedure was done for each swirl case at each location and the results are shown in Figure 4.25. Although the figure portrays a possible slight benefit with the swirling jet cases, not much difference exists. The error in the zero value due to stray light that was not accounted for in the background images, as was discussed in Section 3.2, is also plotted to give an idea of the error of the plotted values.

4.3.2 Thresholded Images

To determine the cross-sectional area of the duct containing some fraction of fuel, the water-seeded fuel images were thresholded, with any intensity value in the image above a cut-off value being assigned a value of one and the rest of the image being assigned a value of zero. The region with intensity values above this cut-off value was defined to be the area containing fuel. Choosing a cut-off value was not easy since the light intensity in the water-seeded jet-mixing region varied greatly between images due to the inability to seed the fuel with a constant amount of water. For some of the images little difference existed between the intensity value in the water-seeded jet-mixing region and the freestream region, while for other images this difference was great. To attempt to have all the images on an equal scale for comparison, each image was rescaled. The most likely to occur value of intensity in the freestream region, as determined by finding the freestream region peak in a histogram of the image, was set to a value of zero, while the most likely to occur intensity value in the water-seeded jet-mixing region was set to a value of 255, with the rest of the image undergoing a linear scaling between those values. The cut-off value was chosen to be 100. This method was not very sensitive to the arbitrary value of 100 chosen. An example of an image thresholded in this manner is shown in Figure 4.26.

Averaging a sequence of thresholded images yields an image of the percentage of time an area will have fuel in it. Figures 4.27 and 4.28 show such averaged thresholded images for all three swirl cases with air and helium fuel at $x/d_j=23.8$. Again, no images exist for the high-swirl case with air fuel. Some of the images are dusty due to low light levels in the jet-mixing region, which caused some of the

30

freestream region to be selected by the threshold method described earlier. This was unavoidable, since if a higher threshold cut-off value was used, some of the region containing fuel would not have been selected. The stray areas at the top of the images are due to condensation in the mixing layer between the cold duct flow and the humid ambient laboratory air, and should be ignored. By comparing the total area that contains fuel in each image (any region not completely black), more spreading of the fuel is evident in the low-swirl and high-swirl cases than the straight case for both fuels. Also, by comparing the brightest region of these images (the completely white region), it can be seen that a larger region of the flow has fuel in it at all times in the low-swirl and high-swirl cases. It is also noted that the helium fuel penetrates farther and spreads wider into the flow than the air fuel. This is probably due to the greater molar rate of helium fuel injection than air fuel injection (refer to Table 3.1).

The twice matched pressure images were also thresholded in the above manner. Figure 4.29 shows the averaged thresholded images at the cross-sectional locations for the straight case with air fuel at matched pressure for comparison against Figure 4.30, which gives the averaged thresholded images for the straight case with air fuel at twice matched pressure. Recall that the twice matched pressure data needs to be scaled for comparison with the matched pressure data due to the differences in the mass flow rates. Thus the twice matched pressure data at $x/d_j=23.8$ should be compared to the matched pressure data at $x/d_j=15.8$ and length dimensions of the twice matched pressure images should be rescaled by a factor of $1/\sqrt{2}$. It is not possible to tell, just by looking at the images, whether there would be any significant difference in the images after rescaling.

To attempt to quantitatively compare the cross-sectional area of the jet-mixing

31

region, the area of each single shot image which contained fuel was calculated from the thresholded images and averaged over all images in a sequence. The results for air and helium fuel are shown in Figures 4.31 and 4.32. A slight increase in the total amount of area containing fuel is seen for the swirling jet cases and the twice matched pressure case at the third cross-sectional location. Note that the stray condensation regions at the top of some of the thresholded images was not included in the total area calculations, and only minimal stray background areas were, which should not greatly affect these results.

Another method of comparison is to look at the penetration occurring in these images. The z/d_j location of the center of mass of the region containing some fraction of fuel, as depicted in the thresholded images, was computed and is shown in Figures 4.33 and 4.34. Penetration appears to be slightly farther for the straight case with air fuel, but very little difference exists between the cases with helium fuel. Penetration for the twice matched pressure case has increased, but recall that the mass flow rate is twice as large as that of the matched pressure case, which should be considered.

4.4 Mixing Layer Growth

As discussed in Section 3.4, images were acquired with the fuel jet discharging into the stagnant laboratory air (no main flow through the duct) such that its exit pressure was matched to atmospheric. The purpose was to determine the effect of fuel molecular weight on mixing layer growth rate. Figure 4.35 shows the results for the straight and low-swirl cases with air fuel and Figure 4.36 shows the same with helium fuel. The fuel was seeded with water to promote condensation in the mixing layer. The images were taken at the side view, and part of the model can be seen at both the bottom of the image

32

and the left side. A piece of tape is seen at the top of the left side of Figure 4.36(a) which was used to prevent the camera from receiving glare from the duct wall that was opposite the fuel injection wall. By comparing the figures for the straight case it is seen that the helium fuel mixes as well as the air fuel, and possibly slightly better. This is consistent with the calculation of Appendix B (based on the theory and correlations of Papamoschou and Roshko[1,16]), which predicts a mixing layer growth rate of $\delta' \approx 0.078$ for air and $\delta' \approx 0.095$ for helium. A great increase in mixing is seen in the low-swirl case over the straight case, both with air and helium fuels, especially near the fuel wall. Since increased mixing with helium fuel is seen, and centrifugal effects suggest the opposite, other effects must be contributing to this phenomenon. The air-in-air results are consistent with earlier, more quantitative studies (such as Reference 5) but the results for helium-in-air with swirl are new and confirm that differences between the air and helium fuel results for injection of fuel into the Mach 2 freestream flow are not attributable to differences in centrifugal effects.

4.5 Discussion

Thus far all comparisons between cases have been made on the basis of equal injector exit diameters. A comparison on the basis of equal mass flow injection rates or one on the basis of equal jet penetration may be more appropriate. Comparison on the basis of injection of equal mass flow rates of fuel might be appropriate for a scramjet combustor with a single fuel injector and the desire to fuel the combustor to a specified fuel-to-oxidant ratio. Comparison on the basis of equal penetration of the fuel might be appropriate where an array of similar injectors existed at a given x-location in a large

aspect ratio combustor and it was desired to fuel the combustor to the centerline (or to the opposite wall if no injectors existed on that wall). Comparisons on these bases deserve some consideration.

With addition of swirl, less fuel is injected for a given fuel jet exit pressure and nozzle contour. To maintain equal mass flow rates as that of the straight case, larger exit diameters would be required for the low-swirl and high-swirl cases. Since equal exit diameters were used for acquisition of the data for all cases, the low-swirl and high-swirl data must be rescaled to account for the difference in mass flow rates. This was done by non-dimensionalizing with the length scale $d_{eff,j}$, the exit diameter of the straight jet with matched pressure which provides the same mass flow rate as actually occurs in the jet, rather than d_j, the actual jet exit diameter. Note that in rescaling and comparing the data in this manner it is assumed that the effects of the confinement by the walls of the duct are not important. Figure 4.37 is a plot of the mean mole fraction of air in the jet-mixing region of the flow (as discussed in Section 4.3.1) with the data rescaled for comparison on the basis of equal mass flow rates. This figure portrays almost no difference in the mean air mole fraction in the jet-mixing region for any case, thus seeming to indicate no benefit from swirling the jet. However, even though the jet-mixing region is apparently mixed to the same extent for any case, the area that the jet-mixing region encompasses is different for each case, being larger for the swirling jet cases (see below). It should be noted that where the mean mole fraction of air is 0.704 (refer to Appendix C) in the jet-mixing region, all the fuel could burn if it were hydrogen (assuming the fuel and air are mixed homogeneously in this region). This condition is seen in these plots to be approached by $x/d_{eff,j} \approx 30\text{-}35$.

34

Figures 4.38 and 4.39 show the average cross-sectional area of the jet-mixing region with the low- and high-swirl data scaled to account for the difference in the mass flow rates. The area for the swirling jet cases is much larger than that of the straight case, especially with the helium fuel, when compared on this basis. The twice matched pressure case, however, shows no increase in area over the matched pressure straight case. The increase in the average cross-sectional area of the jet-mixing region with swirl appears to contradict the results for the streamwise development of mean mole fraction of fuel in the jet-mixing region (for helium fuel, after rescaling). The implication, if we assume similar axial velocity distributions in the jet-mixing region, is a greater mass flow rate of fuel in the swirling cases whereas, in fact, the data are rescaled and presented on the basis of equal fuel jet mass flow rates. This contradiction can be explained in two different ways. First, if the axial velocity in the jet-mixing region were less in the swirling cases and the mole fraction of helium were the same then a greater area of flow would be required ($\dot{m} = \int \rho u \, dA$), as was observed. Second, if there were a total number density decrease in the jet-mixing region in the swirling jet cases this would be interpreted in error as a higher mole fraction of helium. Such a change in number density could occur due to a pressure decrease, such as in the core of a vortex, or by a temperature increase as a result of reduced velocity. Reality probably lies between these two extremes, since there is in fact a portion of the jet-mixing region which lies close to the fuel injection wall in the swirling cases which is absent without swirl. Within this region the axial velocity is presumably lower than elsewhere and the total number density is also presumably lower (increased temperature) due to wall effects. It is therefore concluded that there is a significant increase in mixing with swirl addition and that the

35

results for the mole fraction of helium in the jet-mixing regions are in error in the swirling cases.

The penetration plots were also rescaled to account for the different mass flow rates, with the results shown in Figures 4.40 and 4.41. The results for air fuel seem to indicate a slight increase in penetration for the straight case, with little difference between the matched and twice matched pressure cases. However, with helium fuel penetration is similar for all cases, increasing only slightly for the swirling jet cases. Comparison on the basis of equal penetration would be appropriate if the main objective were to mix to a certain location. Penetration, as portrayed in Figures 4.40 and 4.41, is seen to be similar for all cases when compared on the basis of equal mass flow rates. Thus comparing on the basis of equal penetration produces similar results as comparing on the basis of equal mass flow rates.

It is apparent that the addition of swirl significantly increases the mixing of 30° wall jets. However, it should be mentioned that this comes at some cost, since the jet stagnation pressures (jet plenum pressures) were higher in the swirling jet cases, while the axial components of velocity and hence the direct specific thrust of the fuel jets were calculated to be almost the same with and without swirl.

5.0 Conclusions

The effects of swirl upon mixing of fuel injected from a 30° wall jet into a Mach 2 flow in a constant area duct were investigated in a non-reacting experiment. Swirling fuel jets were generated by tangential injection into a cylindrical swirl chamber followed by axial acceleration through a convergent-divergent nozzle. The fuel was injected such that its static pressure matched the effective back pressure of the main flow. Three cases were considered, a low-swirl, a high-swirl, and a straight (non-swirling) case, and both helium and air were used to simulate fuel. Rayleigh scattering allowed the visualization of the flow with helium fuel, and seeding the fuel with water allowed the spreading of fuel to be visualized for both air and helium fueled cases. Calculating histograms of the pure molecular Rayleigh scattering images and isolating the portion of the histogram that was due to the jet-mixing region of the image allowed the helium concentrations in this region to be monitored. These results showed that the helium concentration was slightly lower for the swirling cases, indicating slightly better mixing. Thresholding the water-seeded images defined the average cross-sectional area of the image containing fuel (the jet-mixing region). A slight increase in this area was found in the swirling jet cases. However, penetration, defined as the mean distance of the fuel from the injection wall, was about the same for all cases with helium fuel, and was slightly less for the low-swirl case than the straight case with air fuel. The data were then rescaled for comparison on the basis of equal mass flow injection. On this basis, almost no difference was found in the air and helium concentrations in the jet-mixing region of the flow, however, a substantial increase in the size of the jet-mixing region was found for the swirling jet case. This increase indicates that the calculated helium concentrations are in error, being

overpredicted for the swirling jet cases, and thus that mixing is indeed increased by swirl. Penetration was only slightly better for the swirling jet cases, with most additional mixing occurring laterally. Data were also collected for the straight case with the fuel injected at twice matched pressure, to determine if increasing pressure had similar benefits to swirl (which requires increased pressure to generate). It was found, when compared on the basis of equal mass flow injection, that no benefit occurred in mixing or penetration for this case.

Improvement in total spreading of the fuel, but not in penetration, was found with swirl. It is believed that this was because, for the straight case, two counter-rotating vortices formed which interacted and caused the fuel to move outward from the fuel injection wall, while in the swirling jet cases one vortex was of much greater strength than the others, which resulted in the jet-mixing region moving towards one side, as opposed to outward, through interaction of the strong vortex with its image in the wall. It is suggested a pair of closely spaced swirling jets with opposite rotation might interact to increase penetration, and that this should be studied in future experiments.

Appendix A: Particle Size Calculation

For Rayleigh scattering of polarized light from a particle viewed at 90° to the plane of polarization,

$$\frac{d_p}{(\lambda/n)} < 0.1 \qquad (A.1)$$

is assumed, and thus

$$\left(\frac{d\sigma}{d\Omega}\right)_{particle} = \frac{16\pi^4}{\lambda^4}\left[\frac{n^2-1}{n^2+2}\left(\frac{d_p}{2}\right)^3\right]^2 \quad \frac{m^2}{steradian} \qquad (A.2)$$

(as given in Reference 20) where d_p is the diameter of a particle, λ is the light wavelength, n is the particle material refractive index and $d\sigma/d\Omega$ is the differential Rayleigh scattering cross-section per unit solid angle Ω. For air, the Rayleigh scattering cross-section is

$$\left(\frac{d\sigma}{d\Omega}\right)_{air} = \frac{4\pi^2\left(n_{STP}-1\right)^2}{N_{STP}^2\,\lambda^4} \qquad (A.3)$$

(as given in Reference 21), where N_{STP} is the number density of air particles at standard temperature (0 °C) and pressure (1 atm). For water (ice) $n \approx 1.31$ and for air at STP $n = 1.0002926$ (as found in Reference 22). In the current experiment $\lambda = 266$ nm, thus

$$\left(\frac{d\sigma}{d\Omega}\right)_{particle} = \frac{16\pi^4}{(266x10^{-9})^4}\left[\frac{1.31^2-1}{1.31^2+2}\cdot\frac{1}{8}\right]^2 d_p^6$$

$$= 1.8063x10^{26}\,d_p^6 \quad \frac{m^2}{steridian} \qquad (A.4)$$

and

$$\left(\frac{d\sigma}{d\Omega}\right)_{air} = \frac{4\pi^2\left(1.0002926-1\right)^2}{(2.6883x10^{25})^2\,(266x10^{-9})^4}$$

$$= 9.342x10^{-31} \quad \frac{m^2}{steradian} \qquad (A.5)$$

where N_{STP} was calculated as

$$N_{STP} = \frac{101325 \; N/m^2}{8314.3 \; \dfrac{J}{kgmol \; K} * 273 \; K} * 6.0222x10^{26} \; molecules/kgmol$$

(A.6)

$$= 2.6883x10^{25} \; \frac{molecules}{m^3}$$

The ratio of water particulate scattering to air molecular (gaseous) scattering, S, is given by

$$S = \frac{\left(\dfrac{d\sigma}{d\Omega}\right)_{particles} N_d}{\left(\dfrac{d\sigma}{d\Omega}\right)_{air} N} = \frac{1.8063x10^{26} \; d_p^6 \; N_d}{9.342x10^{-31} \; N}$$

(A.7)

where N_d is the number density of particles with diameter d_p and N is the number density of air molecules. Now,

$$d_p = \left(\frac{9.342x10^{-31}}{1.8063x10^{26}} \cdot \frac{N \; S}{N_d}\right)^{\left(\frac{1}{6}\right)} = 4.159x10^{-10}\left(\frac{N \; S}{N_d}\right)^{\left(\frac{1}{6}\right)} \; m$$

(A.8)

The number of particles viewed per pixel of CCD camera is related to r.m.s. noise. Assuming all particles are equally bright and camera read noise is zero, pixel noise is given by Poisson statistics:

$$sn = \frac{mean \; pixel \; signal}{r.m.s. \; pixel \; signal} = \sqrt{n_p}$$

(A.9)

where n_p is the mean number of particles viewed in a given pixel. For a field of view of height L with number of pixels P in the field of view,

$$h = \frac{L}{P_n}$$

(A.10)

where h is the height imaged on one pixel. Thus, since the pixels are square

$$N_d = \frac{n_p}{h^2 t} = \frac{sn^2}{\left(\frac{L}{P_n}\right)^2 t} \qquad \text{(A.11)}$$

where t is the light sheet thickness. For a diffraction-limited Gaussian beam with diameter of the beam at the lens D, focal length f, and beam waist $2w_0$ at the focal point,

$$t = 2w_o = \frac{4\lambda}{\pi} \frac{f}{D} \qquad \text{(A.12)}$$

where D and $2w_0$ are measured to the e^{-2} intensity point. For f=39 inches and D=10 mm,

$$2w_o = \frac{4 * 266x10^{-3} \ \mu m * 39 \ inches * 25.4 \ mm/inch}{\pi * 10 \ mm} \qquad \text{(A.13)}$$

$$= 33.5 \ \mu m$$

This is the smallest the light sheet thickness could be. Since a perfect diffraction-limited Gaussian beam does not exist in the current experiment, the thickness of the light sheet is estimated to be 100 μm. For L=1.5 inches, P=255 pixels, and t=100 μm

$$N_d = \frac{sn^2}{\left(\frac{1.5 \ inches * 25.4x10^{-3} \ m/inch}{255}\right)^2 100x10^{-6} \ m} \qquad \text{(A.14)}$$

$$= 4.4795x10^{11} \ sn^2 \ \frac{particles}{m^3}$$

Now, suppose we consider a downstream cross-section. Assume the fuel jet (i.e. region with particles) is at Mach 2, T_0=298 K, p=1 atm.

$$M = 2 \rightarrow \frac{T}{T_o} = 0.5556 \qquad \text{(A.15)}$$

as found in the Ames Tables[23]. Now,

$$N = \frac{101325 \ N/m^2}{8314.3 \ \frac{J}{kgmol \ K} * 0.5556 * 298 \ K} * 6.0222x10^{26} \ \frac{molecules}{kgmol}$$

(A.16)

$$= 4.433x10^{25} \ \frac{molecules}{m^3}$$

Thus,

$$d_p = 4.159x10^{-10} \left(\frac{4.433x10^{25}}{4.4795x10^{11}} \ \frac{S}{sn^2} \right)^{\left(\frac{1}{6}\right)} m$$

(A.17)

$$= 0.08945 \left(\frac{S}{sn^2} \right)^{\frac{1}{6}} \ \mu m$$

The average intensity value in the jet-mixing region of an image with water-seeded helium fuel, normalized by the freestream intensity value, divided by the corresponding value for an image without water-seeding (also normalized by its freestream value) was calculated for many images. This value, which is S, ranged from 8 to 12, depending on the amount of water in the fuel. The signal-to-noise ratio, sn, was calculated by assuming that the time-averaged noise at a particular pixel can be approximated by the noise in a region of an image where intensity should be uniform. Thus the mean and standard deviation in the intensity values of an area of the freestream where intensity should have been uniform (as discussed in Section 3.2) were found, with sn being given as the mean intensity value divided by the standard deviation in that value. This value typically ranged from 18-24. Using $S \approx 10$ and $sn \approx 20$,

$$d_p \approx 0.05 \ \mu m$$

(A.18)

Note that because of the 1/6 power law dependence of d_p on S, sn and t, that relative uncertaintines in d_p due to uncertainties in S, sn and t are less than relative uncertainties in S, sn or t themselves.

42

Appendix B: Mixing Layer Growth Rate Calculations

The growth rate of visual thickness, δ', of a high-speed mixing layer which is two-dimensional in the mean, is given by Papamoschou and Roshko[1,16] as

$$\frac{\delta'}{\delta'_i} \approx f\left(M_{c_1}\right) \qquad (B.1)$$

δ'_i is the growth rate of an incompressible shear layer, where the ratios of the velocities (u_2/u_1) and densities (ρ_2/ρ_1) in the two layers are the same, and is given by

$$\delta'_i = 0.17 * \frac{\left[1-\frac{u_2}{u_1}\right]\left[1+\left(\frac{\rho_2}{\rho_1}\right)^{\frac{1}{2}}\right]}{\left[1+\frac{u_2}{u_1}\left(\frac{\rho_2}{\rho_1}\right)^{\frac{1}{2}}\right]} \qquad (B.2)$$

where subscript 1 refers to the high-speed stream and subscript 2 to the low-speed stream. The convective Mach number, which is the Mach number of the high speed stream in a coordinate system moving with the velocity of the dominant structures of the shear layer $(M_{c,1})$, or the Mach number of the dominant structures in a coordinate system moving with the low-speed stream $(M_{c,2})$, is given by

$$M_{c_1} = \frac{u_1 - u_c}{a_1} \qquad (B.3)$$

where

$$u_c = \frac{a_2 u_1 + a_1 u_2}{a_1 + a_2} \qquad (B.4)$$

and a_1 and a_2 are the speeds of sound of the high- and low-speed streams. The function $f(M_{c,1})$ is observed to fall asymptotically from a value of 1 to a value of about 0.2 as

$M_{c,1}$ rises to about 1. This version of the theory neglects the effects of differences in γ between the two streams, which are not thought to be very large.

Although the experimental mixing layers are not two-dimensional, these formulas were used to approximate $M_{c,1}$ and δ' for the straight jet cases. For the fuel jet exiting with a static pressure of 33 psia into the freestream also at a static pressure of 33 psia, the Mach number of the freestream was estimated by calculating the Mach number over a cone with a 30° semi-vertex angle in a nominal Mach 2 flow. From the Ames tables[23] this Mach number was found to be 1.258 at the fuel injection point. For a total temperature of 290 K the density of the main flow was 1.6024 kg/m³, the speed of sound was 297.54 m/s, and the velocity was 374.301 m/s. The fuel jet has an exit Mach number of 2.197 for the straight case with air fuel and 2.401 for the straight case with helium fuel. This, along with using a total temperature of 290 K, results in a calculated density of 2.392 kg/m³, u=534.9 m/s and a=243.512m/s for air fuel and ρ=0.49142 kg/m³, u=1407.4 m/s, and a=586.2 m/s for helium fuel. The fuel jet is the higher speed stream, and thus designated as stream 1, with the freestream as stream 2. Substituting these values into equations (B.2)-(B.4) yields incompressible shear layer growth rates of 0.05904 and 0.23653 for air and helium fuel, respectively, and convective Mach numbers of 0.29696 and 1.16898. From Figure 10 of Papamoschou and Roshko[1], δ'/δ'_i=0.95 and 0.22 for the two fuels, resulting in a mixing layer growth rate of 0.05314 for air fuel and 0.05913 for helium fuel.

For the case of the jet exiting into the stagnant laboratory air with jet exit pressure matched to the atmosphere (14.7 psia), the freestream conditions are ρ=1.18457 kg/m³, u=0, and a=346.05 m/s, resulting in incompressible shear layer growth rates of 0.28963 for air fuel and 0.43394 for helium fuel and convective Mach numbers of 0.9074 and 1.5096, respectively. Again referencing Figure 10 of Papamoschou and Roshko[1], δ'/δ'_i was found to be 0.27 for air fuel and 0.22 for helium fuel, resulting in growth rates of 0.0782 and 0.095, respectively.

44

Appendix C: Mole Fraction Calculations

The main reaction governing the burning of hydrogen with oxygen is

$$H_2 + \frac{1}{2}O_2 \rightarrow H_2O \qquad \text{(C.1)}$$

If just enough oxygen was mixed with the hydrogen to burn it, and no more, then half a mole of oxygen would be needed for every mole of hydrogen. Since air is 21% oxygen by volume, 2.38 moles of air (which contains half a mole of oxygen) would be needed for every mole of hydrogen to completely burn it. The mole fractions would then be

$$X_{air} = \frac{n_{air}}{n_{H_2} + n_{air}} = \frac{2.38}{1 + 2.38} = 0.704 \qquad \text{(C.2)}$$

and

$$X_{H_2} = 1 - X_{air} = 1 - 0.704 = 0.296 \qquad \text{(C.3)}$$

If it is assumed that a molecule of helium mixes like a molecule of hydrogen, then, where the mean mole fraction of air is 70.4% in the jet-mixing region, all the fuel can burn, assuming the fuel and air are mixed homogeneously.

References

1. D. Papamoschou and A. Roshko, "Observations of Supersonic Free Shear Layer," AIAA Paper 86-1062, 1986.

2. J. Swithenbank and N.A. Chigier, "Vortex Mixing for Supersonic Combustion," *Proceedings Twelfth Symposium (International) on Combustion*, The Combustion Institute, 1969, pp 1153-1162.

3. A.D. Cutler and B.S. Levey, "Vortex Breakdown in a Supersonic Jet," AIAA Paper 91-1815, 1991.

4. B.S. Levey, "An Experimental Investigation of a Supersonic Vortical Flow," Master of Science Thesis, The George Washington University, September 1991.

5. A.D. Cutler, B.S. Levey, and D.K. Kraus, "An Experimental Investigation of Supersonic Swirling Jets," AIAA Paper 93-2922, 1993.

6. J.W. Naughton and G.S. Settles, "Experiments on the Enhancement of Compressible Mixing via Streamwise Vorticity, Part 1 - Optical Measurements," AIAA Paper 92-3549, 1992.

7. D.K. Kraus and A.D. Cutler, "Mixing Enhancement by Use of Swirling Jets," AIAA Paper 93-3126, 1993.

8. J. Delery, E. Horowitz, O. Leuchter, J.L. Solignac, "Fundamental Studies on Vortex Flows," *La Recherche Aerospatiale*, No. 1984-2, 1984.

9. L.N. Cattafesta III and G.S. Settles, "Experiments on Shock/Vortex Interaction," AIAA Paper 92-0315, 1992.

10. C.R. McClinton, "The Effect of Injection Angle on the Interaction Between Sonic Secondary Jets and a Supersonic Free Stream," NASA TND-6669, February 1972.

11. D.W. Riggins and C.R. McClinton, "Analysis of Losses in Supersonic Mixing and Reacting Flows," AIAA Paper 91-2266, 1991.

12. R.B. Mays, R.H. Thomas, and J.A. Schetz, "Low Angle Injection Into a Supersonic Flow," AIAA Paper 89-2461, 1989.

13. P.S. King, R.H. Thomas and J.A. Schetz, "Combined Tangential-Normal Injection into a Supersonic Flow," AIAA Paper 89-0622, 1989.

14. G.B. Northam, I. Greenberg and C.S. Byington, "Evaluation of Parallel Injector Configurations for Supersonic Combustion," AIAA Paper 89-2525, 1989.

15.   S.D. Stouffer, N.R. Baker, D.P. Capriotti and G.B. Northam, "Effects of Compression and Expansion-Ramp Fuel Injector Configurations on Scramjet Combustion and Heat Transfer," AIAA Paper 93-0609, 1993.

16.   D. Papamoschou and A. Roshko, "The Compressible Turbulent Shear Layer: An Experimental Study," *Journal of Fluid Mechanics*, Vol. 197, 1988, pp 453-477.

17.   D.C. Fourguette, M.G. Mungal, and R.W. Dibble, "Time Evolution of the Shear Layer of a Supersonic Axisymmetric Jet," *AIAA Journal*, Vol. 29, No. 7, 1991, pp 1123-1130.

18.   Chia-Shun Yih, "Dual Role of Viscosity in the Instability of Revolving Fluids of Variable Density," *Physics of Fluids*, Vol. 4, No. 7, 1961.

19.   P. Bradshaw, "Effects of Streamline Curvature on Turbulent Flow," AGARD-AG-169.

20.   R. Siegel and J.R. Howell, *Thermal Radiation Heat Transfer*, Hemisphere Publishing Corporation, 1992.

21.   A.C. Eckbreth, *Laser Diagnostics for Combustion Temperature and Species*, Abacus Press, 1988, p 210.

22.   R.C. Weast, M.J. Astle, and W.H. Beyer, *CRC Handbook of Chemistry and Physics*, 69th Edition, CRC Press, Boca Raton, Florida, 1988-89, pp B-94, E-384.

23.   Ames Research Staff, "Equations, Tables, and Charts for Compressible Flow," NACA Report 1135, 1953, p 47.
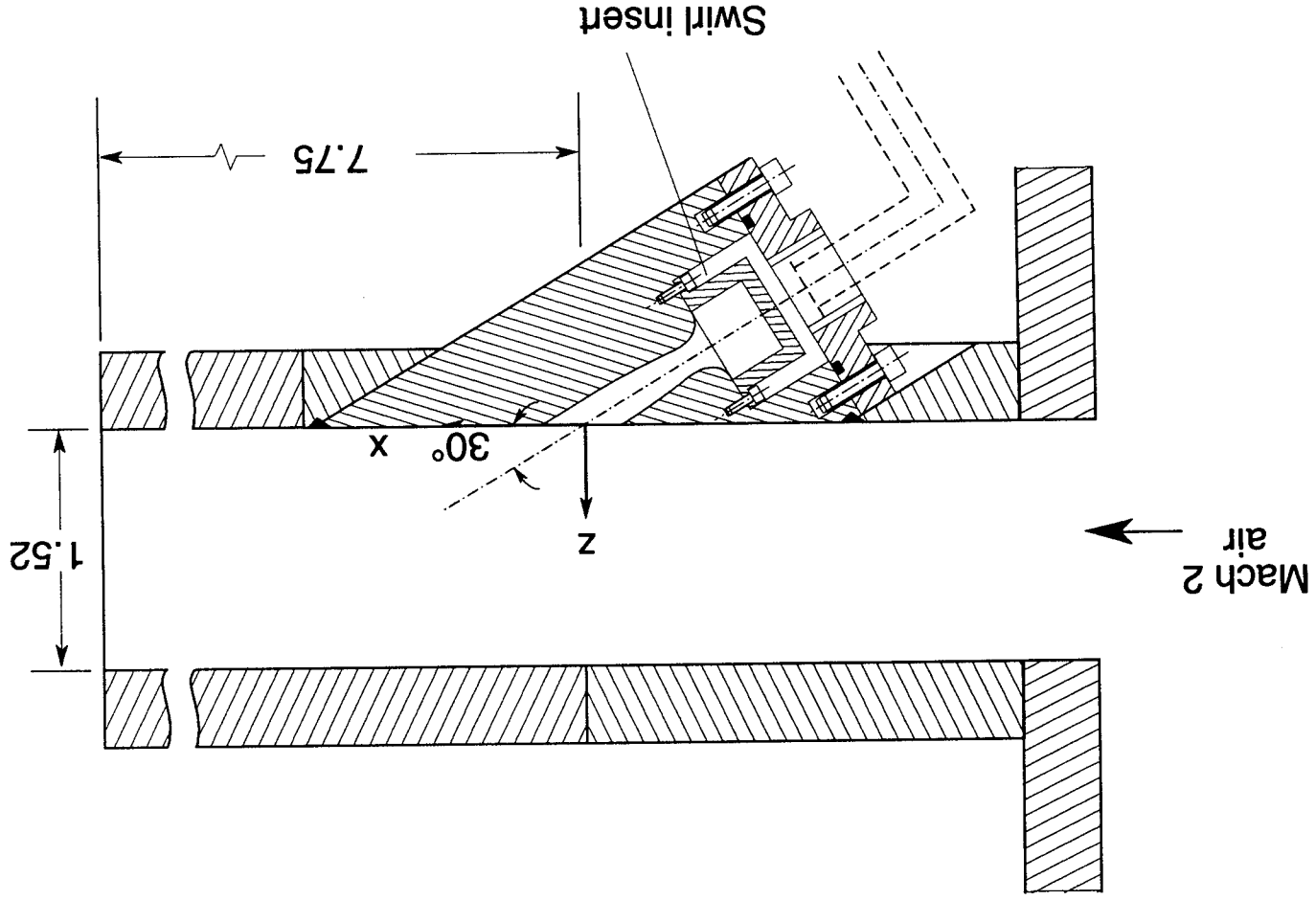
Figure 3.1. Side view schematic of experimental duct.
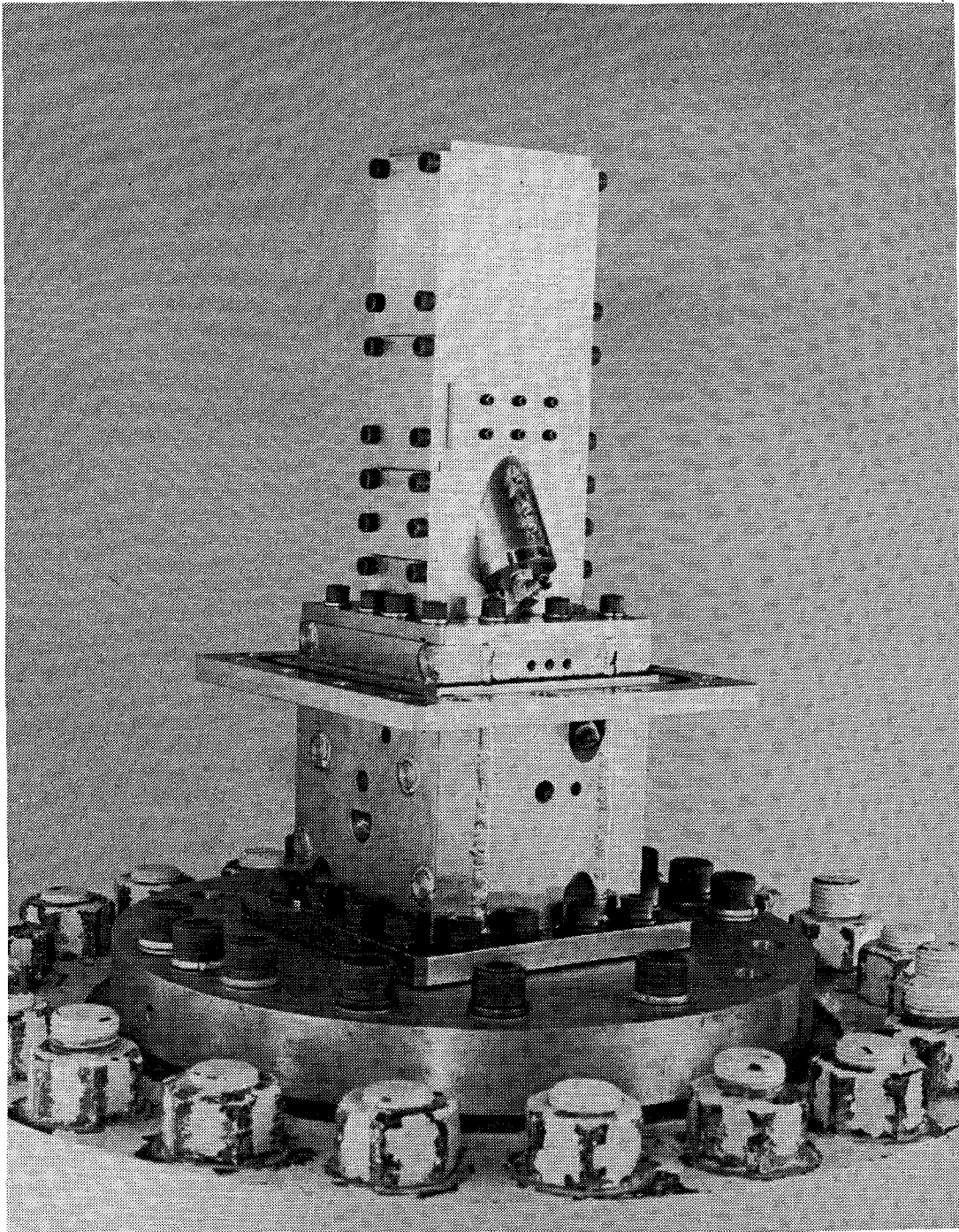
Figure 3.2. Photograph of plenum with nozzle and duct mounted on top.

A

B

Dia 0.1015
(16 holes)

Rad
0.25

(a) straight

A

Dia 0.0550
(16 holes)

Rad
0.25

B

Dimensions in inches

(b) low-swirl

A

Dia 0.0465
(4 holes)

Rad
0.25

B

Section B

Section A

(c) high-swirl
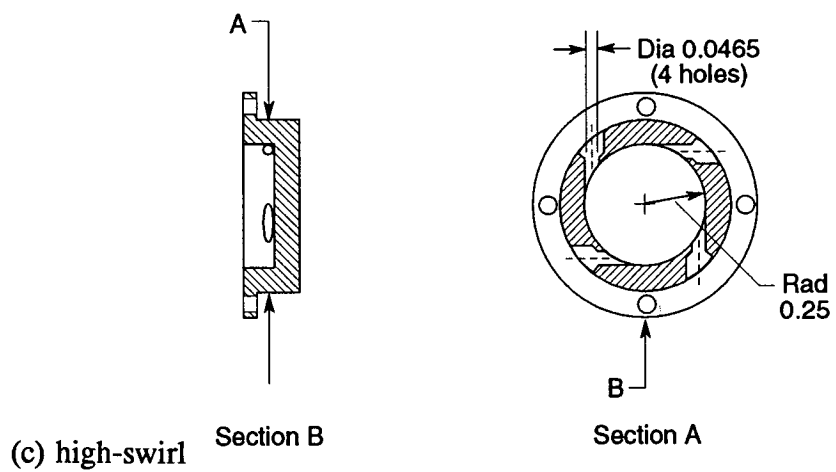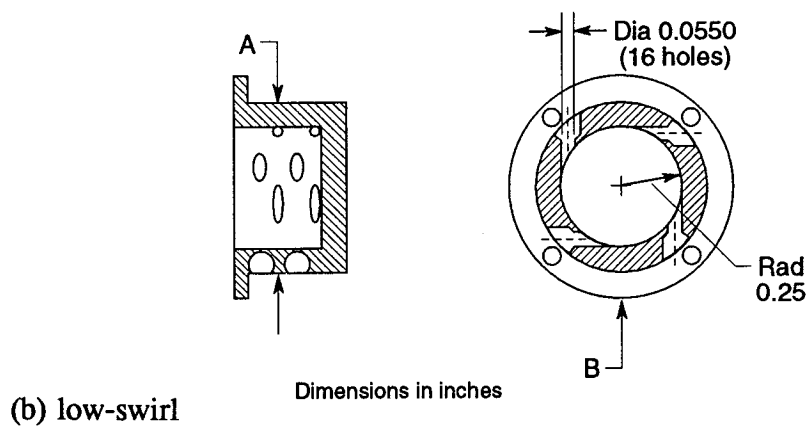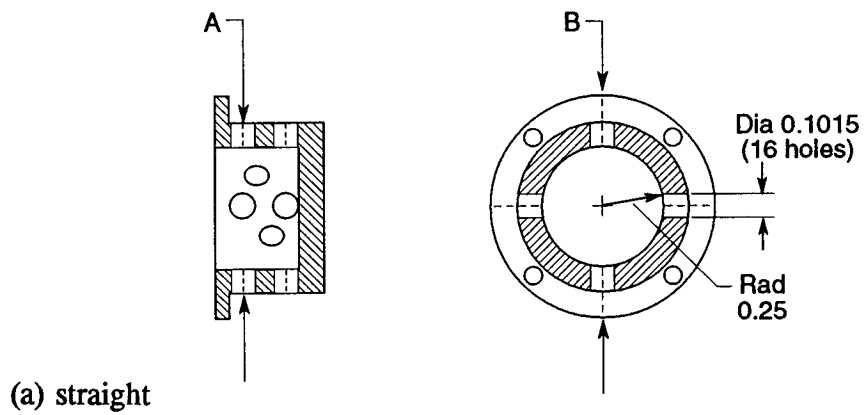
Figure 3.3. Top-hat shaped swirl inserts.
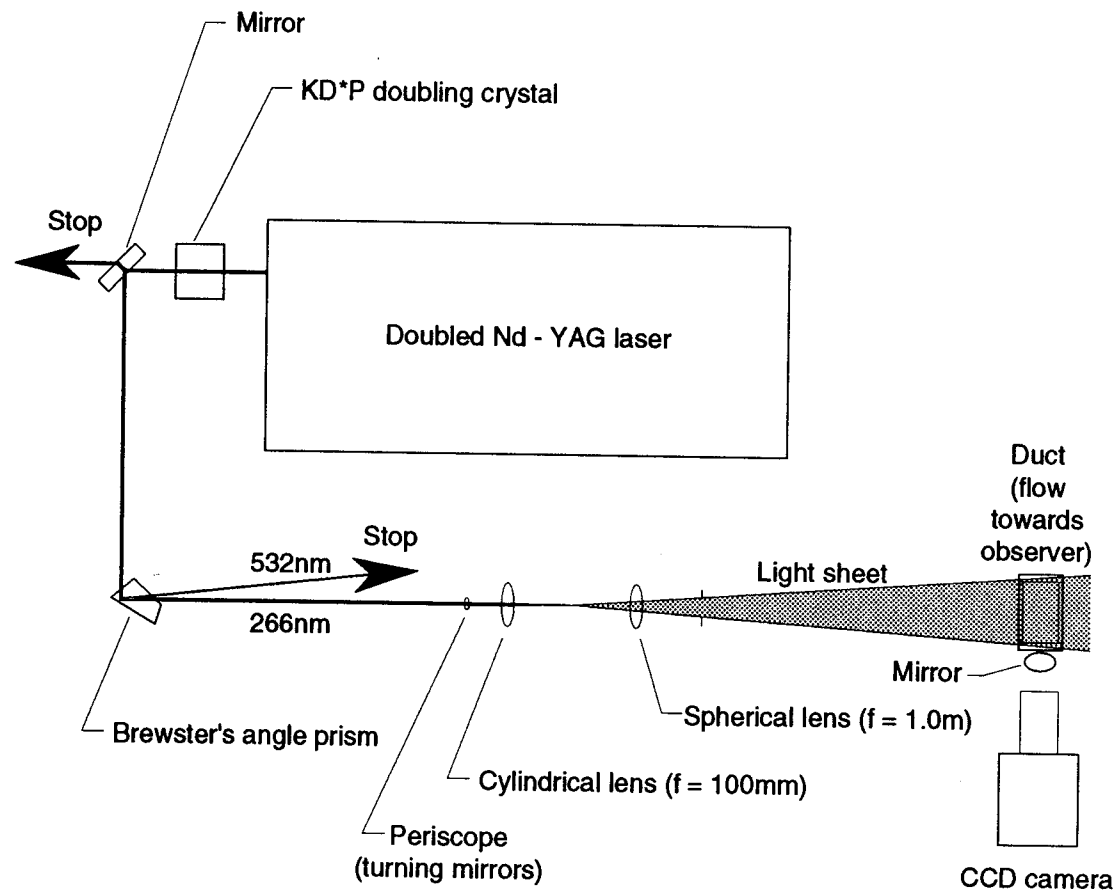
Figure 3.4. Optics layout for Rayleigh scattering flow visualization.
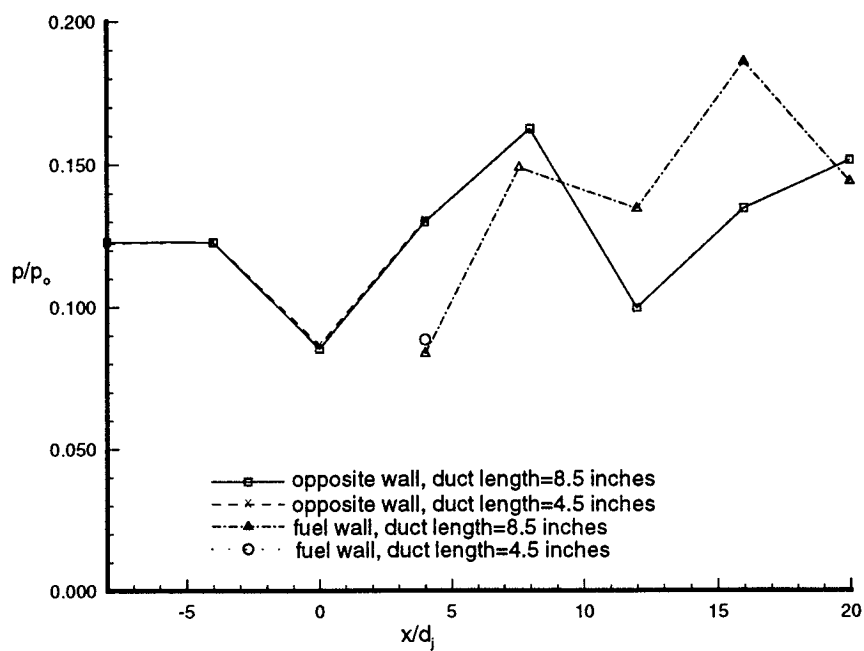
Figure 4.1. Pressure readings along duct walls for straight case.
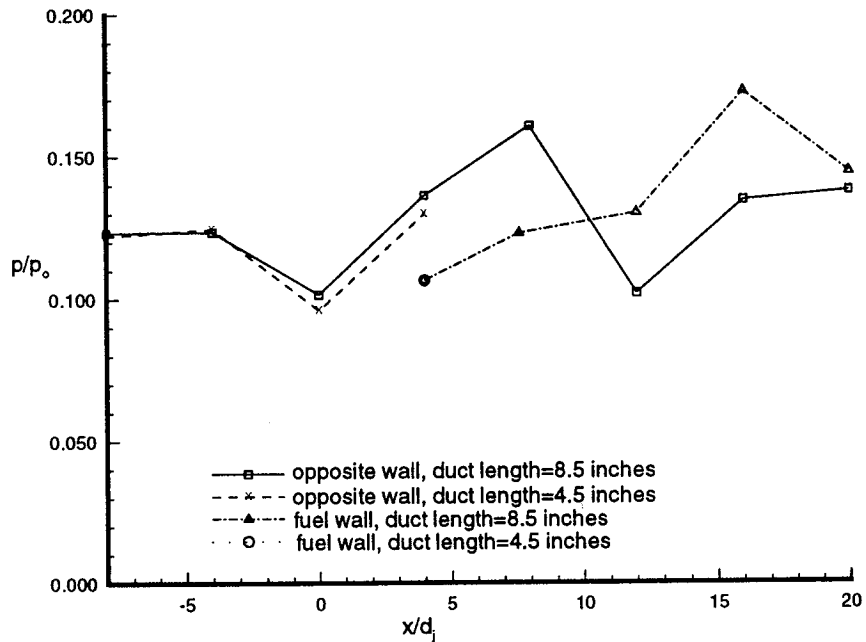
Figure 4.2. Pressure readings along duct walls for low-swirl case.

52
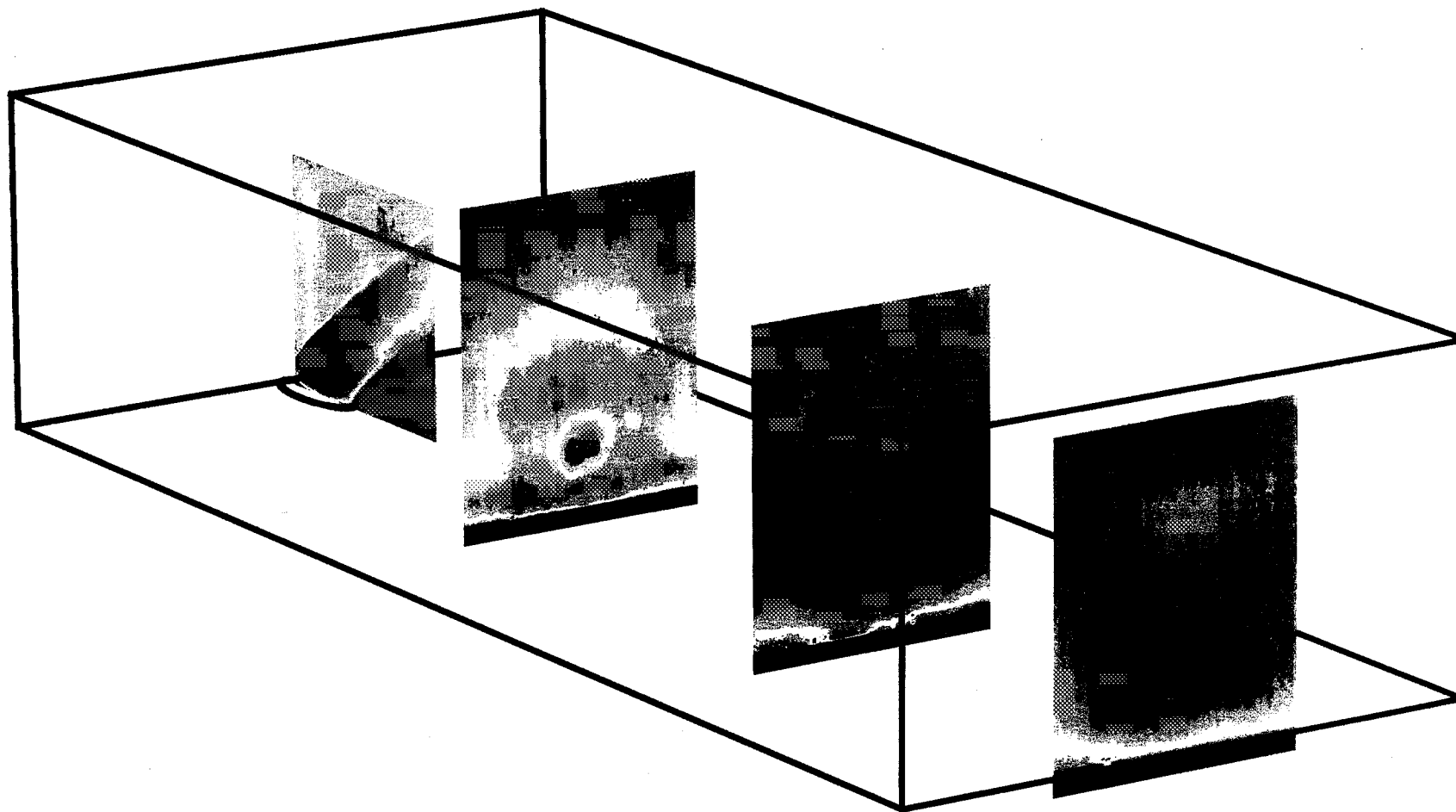
Figure 4.3. Composite view of average Rayleigh scattering images for straight case with air fuel.
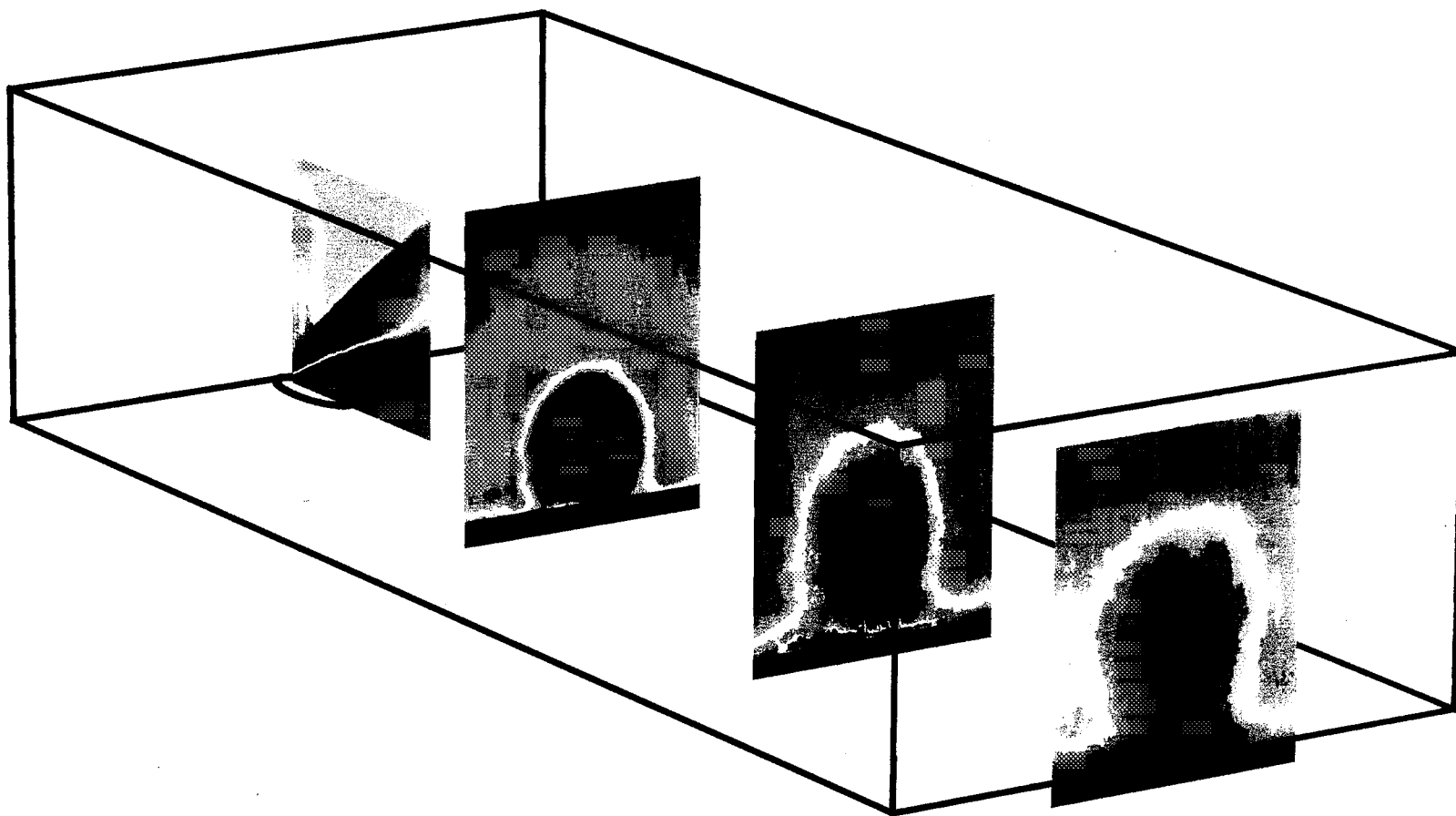
Figure 4.4. Composite view of average Rayleigh scattering images for straight case with helium fuel.
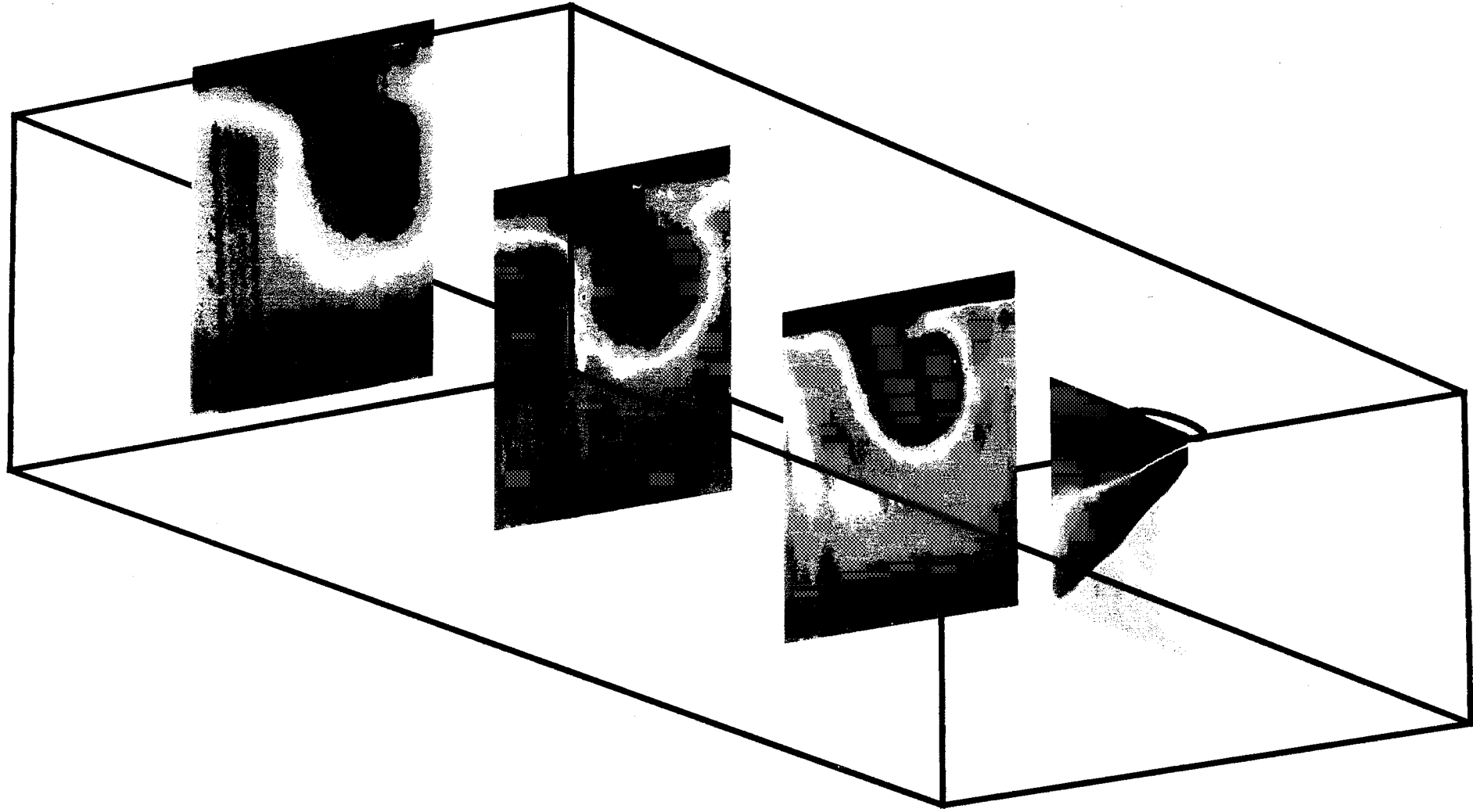
Figure 4.5. Composite view of average Rayleigh scattering images for low-swirl case with helium fuel.

55
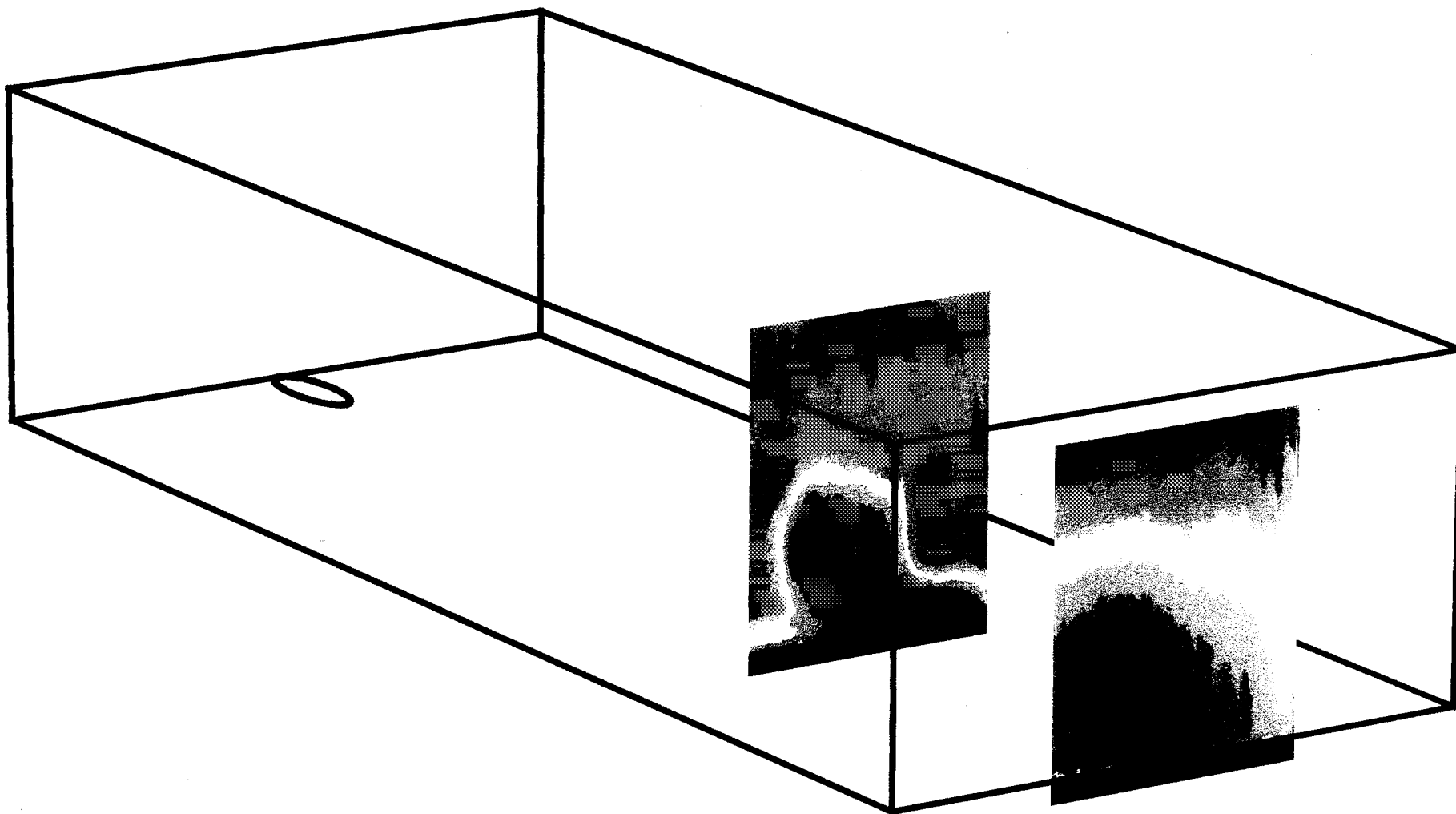
Figure 4.6. Composite view of average Rayleigh scattering images for high-swirl case with helium fuel.

(a) straight case
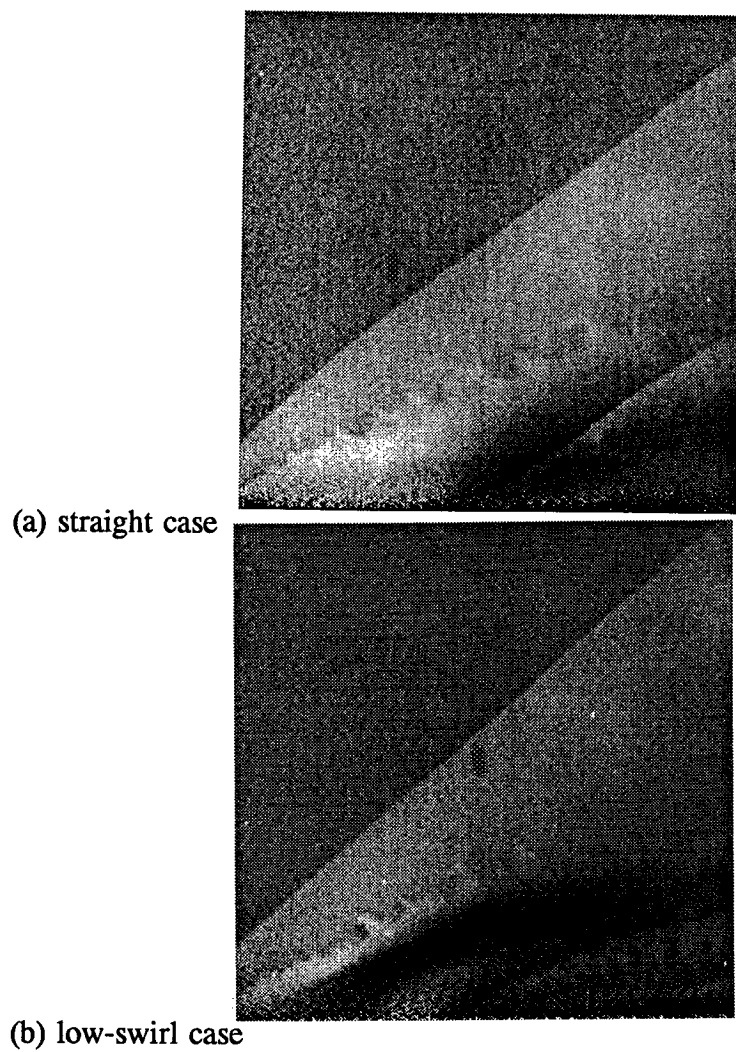
(b) low-swirl case

Figure 4.7. Instantaneous pure Rayleigh scattering images with air fuel at side view.
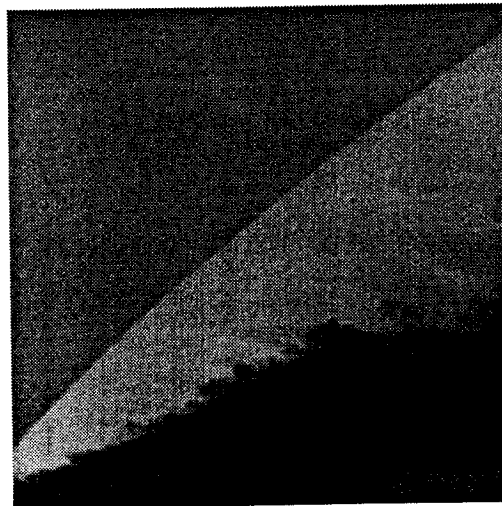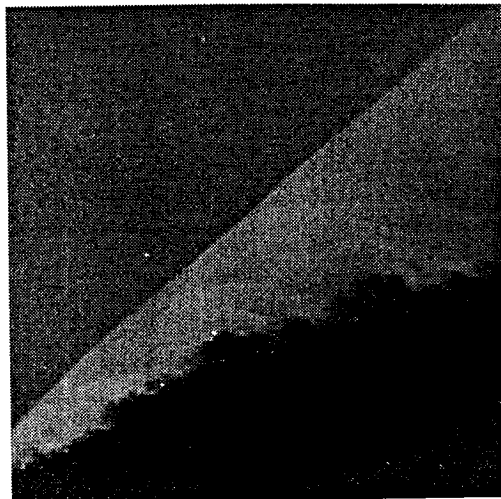
(a) straight case
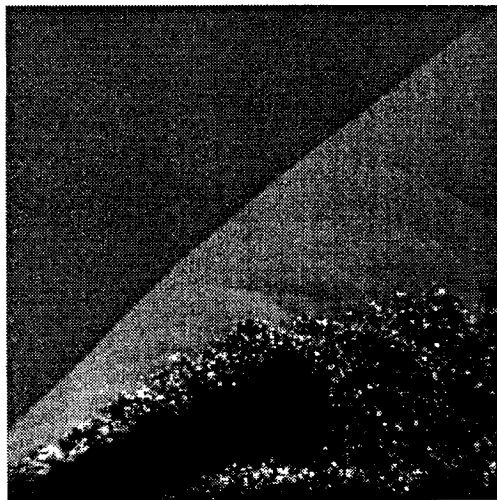
(b) low-swirl case

(c) high-swirl case

Figure 4.8. Instantaneous pure Rayleigh scattering images with helium fuel at side view.

58
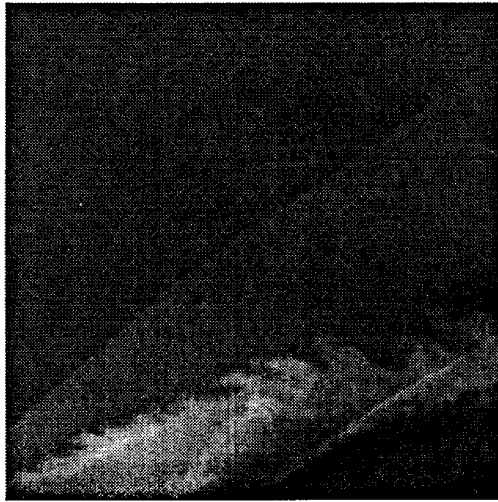
(a) straight case
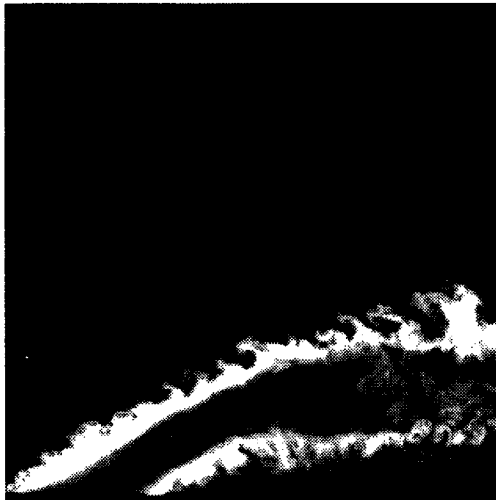
(b) low-swirl case

Figure 4.9. Instantaneous Rayleigh scattering images with water-seeded air fuel at side view.

(a) straight case
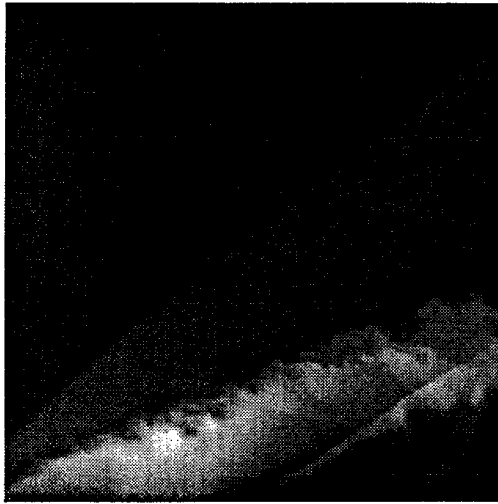
(b) low-swirl case

(c) high-swirl case

Figure 4.10. Instantaneous Rayleigh scattering images with water-seeded helium fuel at side view.
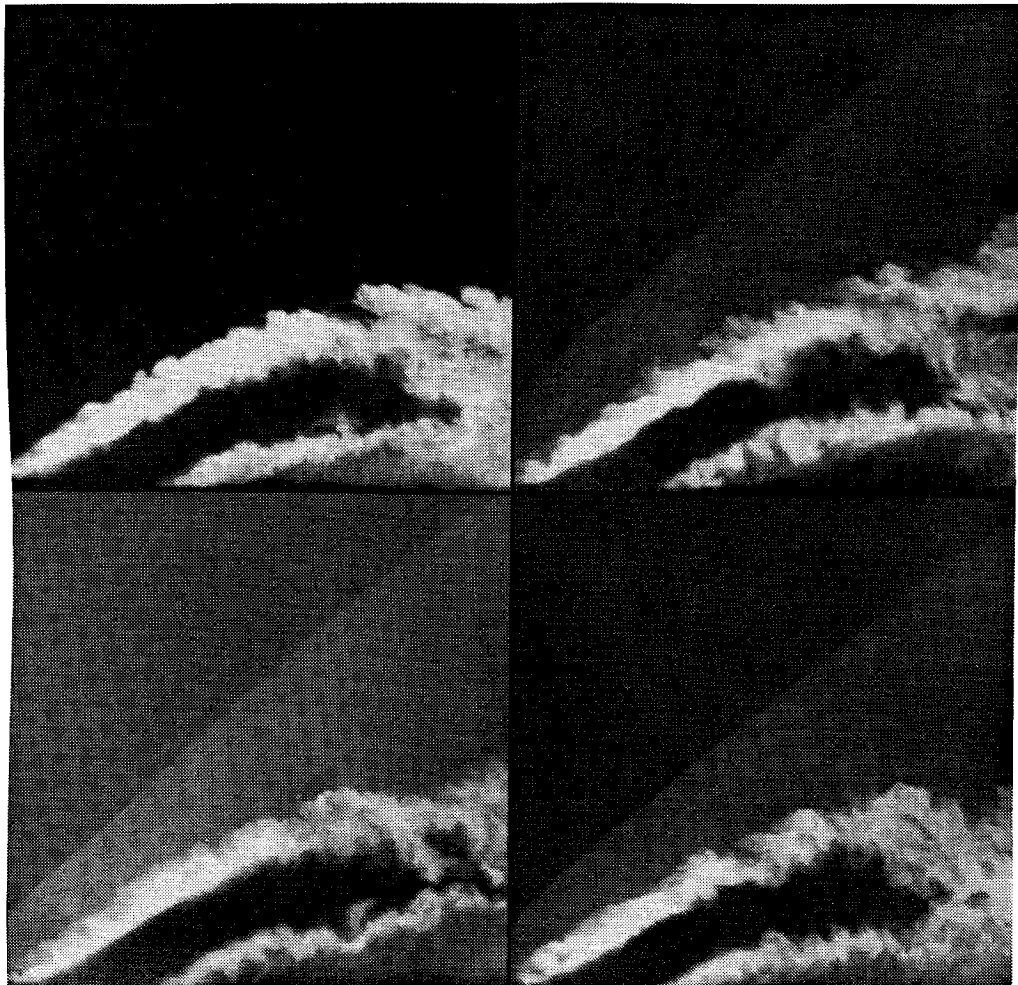
Figure 4.11. Sequence of instantaneous Rayleigh scattering images for low-swirl case with water-seeded helium fuel at side view.

(a) straight case
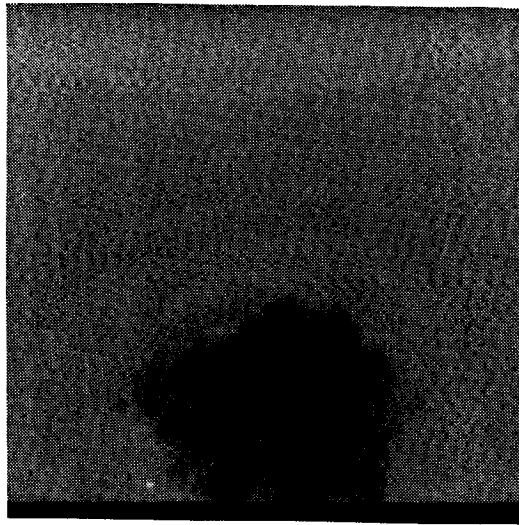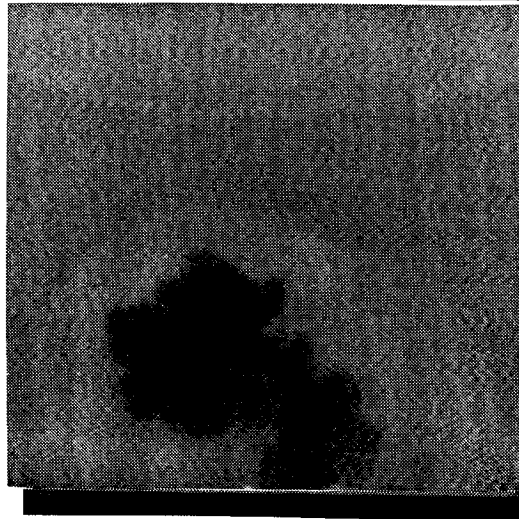
(b) low-swirl case
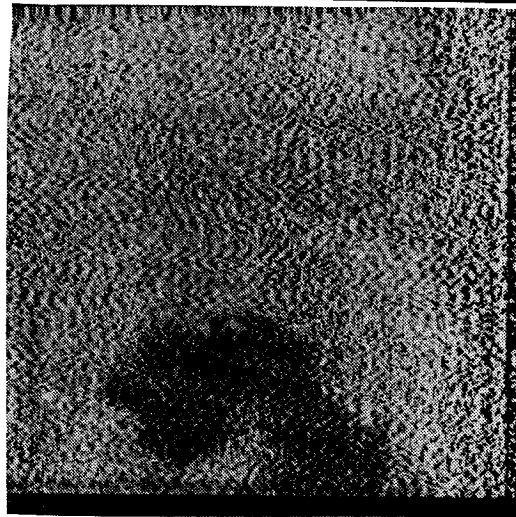
(c) high-swirl case

Figure 4.12. Instantaneous pure Rayleigh scattering images with helium fuel at $x/d_j = 7.8$.

(a) straight case

(b) low-swirl case

Figure 4.13. Instantaneous Rayleigh scattering images with water-seeded air fuel at $x/d_j=7.8$.

(a) straight case
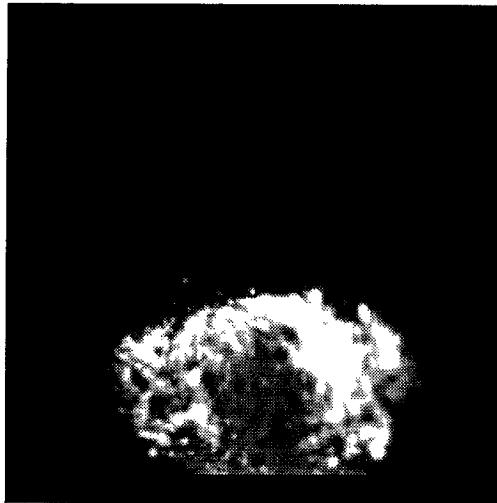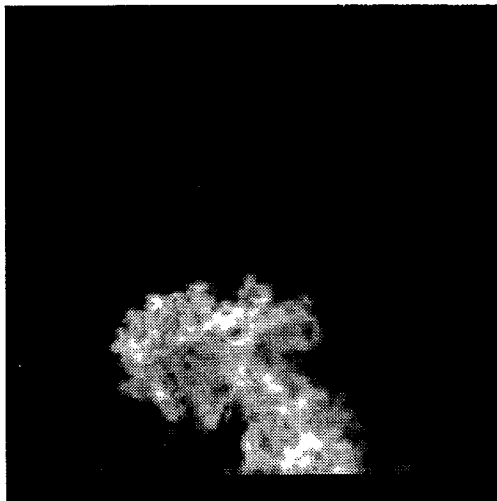
(b) low-swirl case
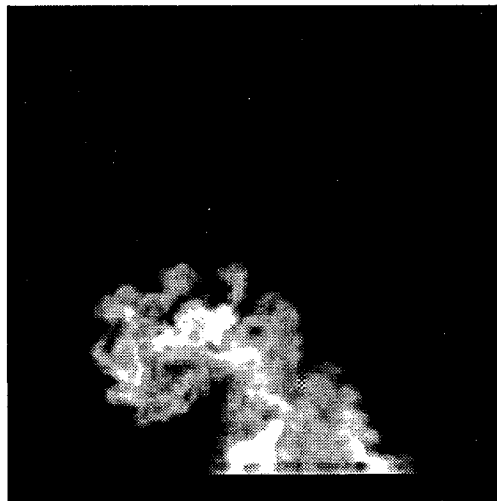
(c) high-swirl case

Figure 4.14. Instantaneous Rayleigh scattering images with water-seeded helium fuel at $x/d_j=7.8$.

(a) straight case
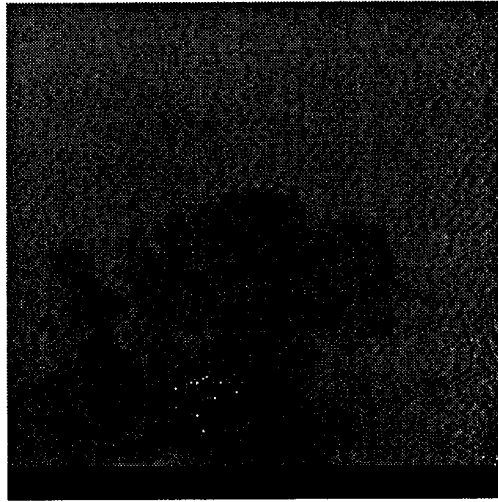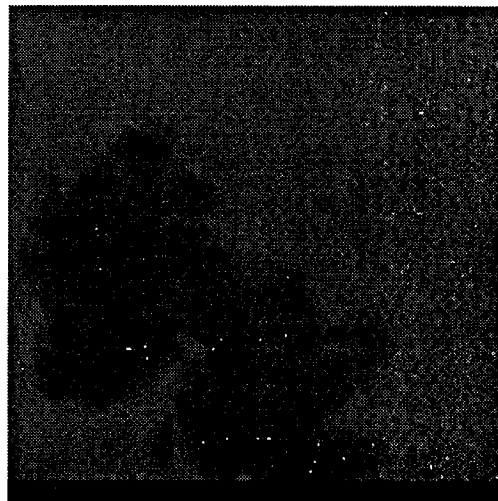
(b) low-swirl case
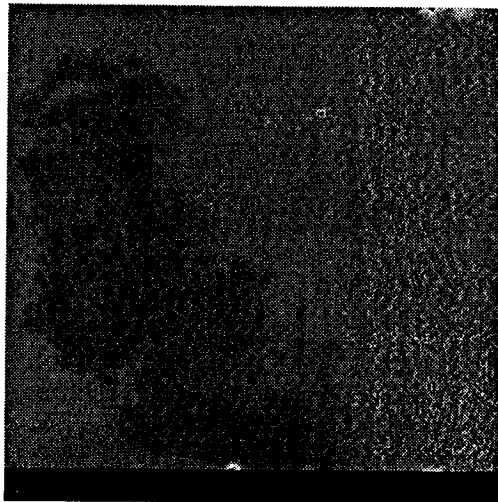
(c) high-swirl case

Figure 4.15. Instantaneous pure Rayleigh scattering images with helium fuel at x/d_j=23.8.
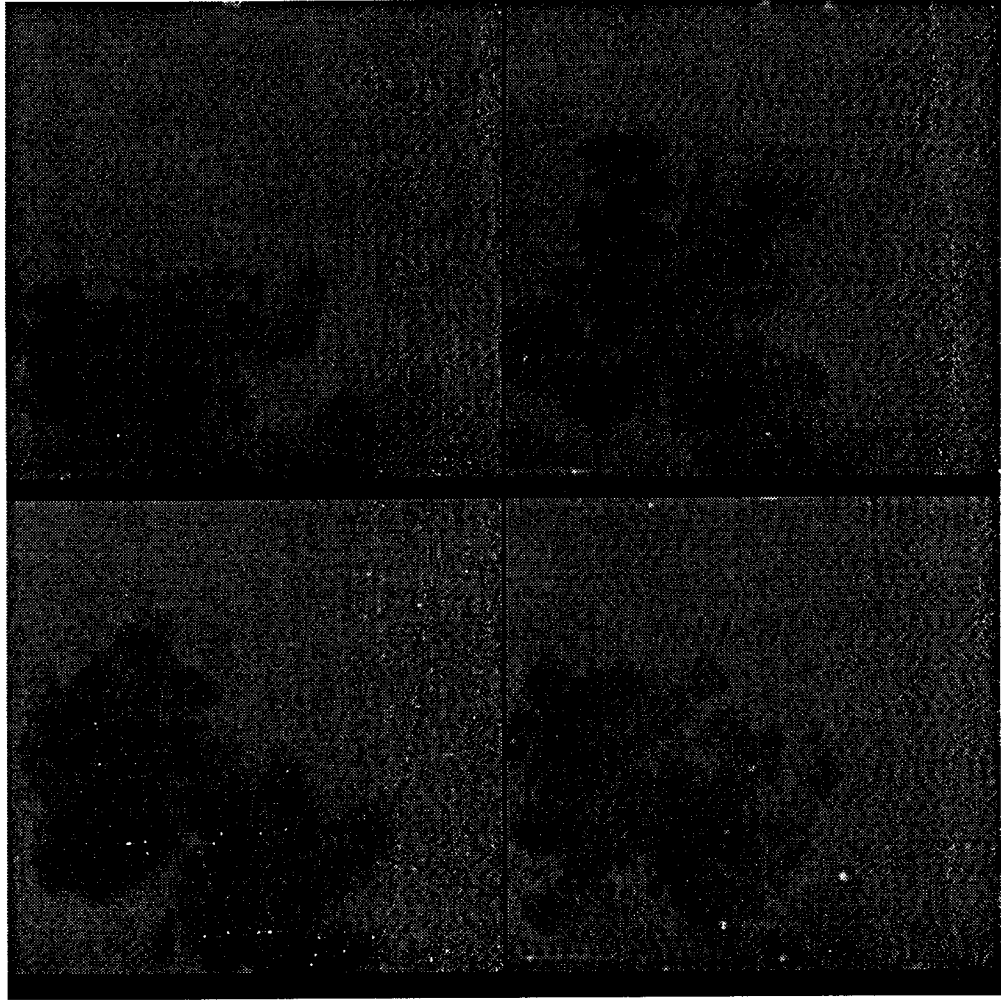
Figure 4.16. Sequence of instantaneous pure Rayleigh scattering images for low-swirl case with helium fuel at x/d_j=23.8.
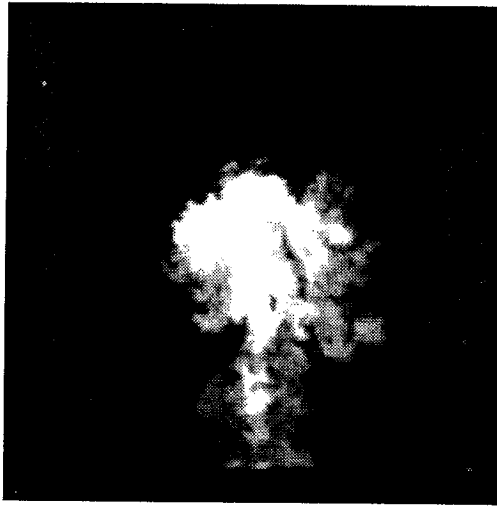
(a) straight case

(b) low-swirl case

Figure 4.17. Instantaneous Rayleigh scattering images with water-seeded air fuel at $x/d_j = 23.8$.

(a) straight case
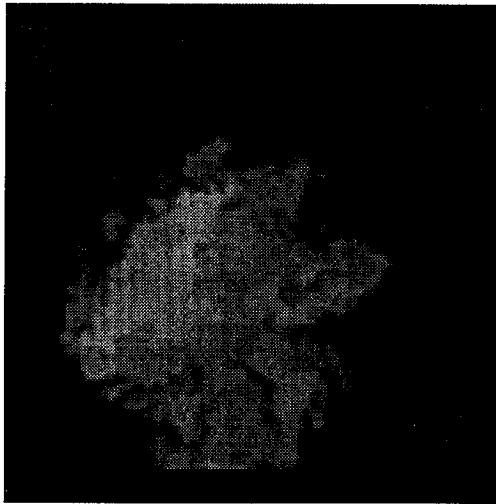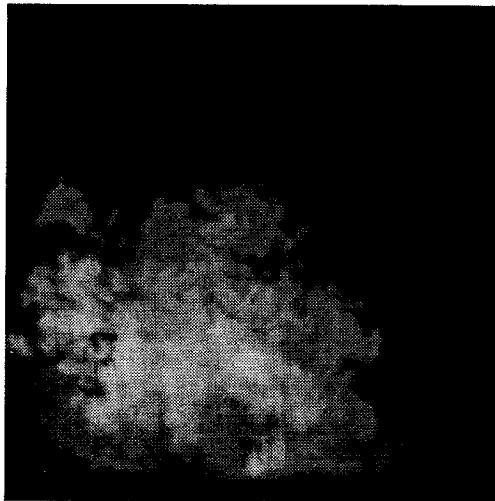
(b) low-swirl case

(c) high-swirl case
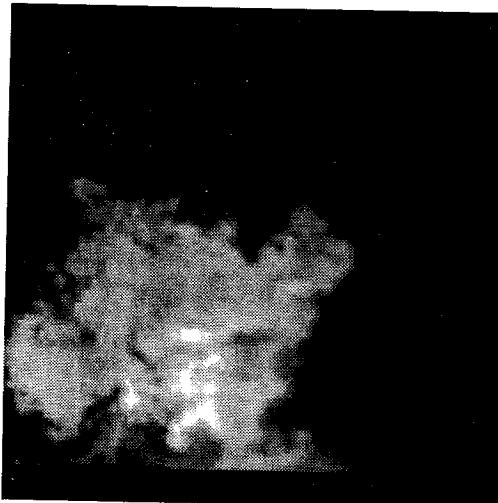
Figure 4.18. Instantaneous Rayleigh scattering images with water-seeded helium fuel at $x/d_j = 23.8$.
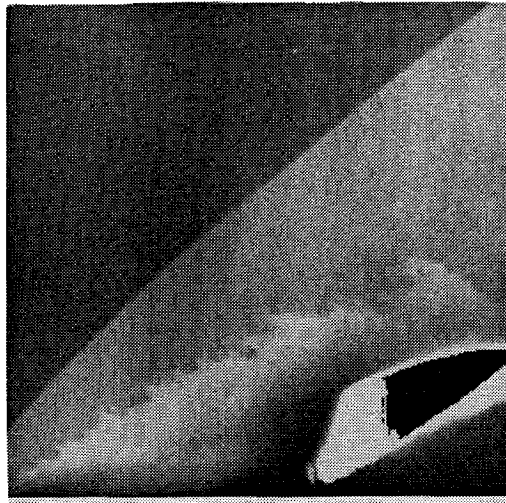
Figure 4.19. Instantaneous pure Rayleigh scattering image for straight case with air fuel at twice matched pressure at side view.
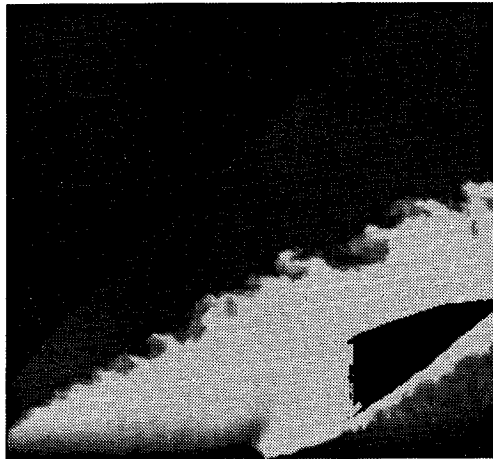
Figure 4.20. Instantaneous Rayleigh scattering image for straight case with water-seeded air fuel at twice matched pressure at side view.

(a) $x/d_j = 7.8$
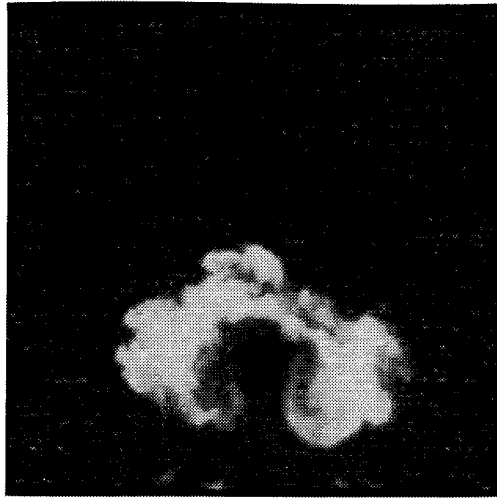
(b) $x/d_j = 15.8$
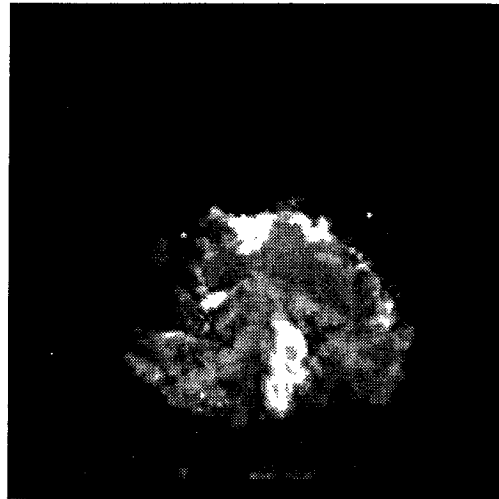
(c) $x/d_j = 23.8$
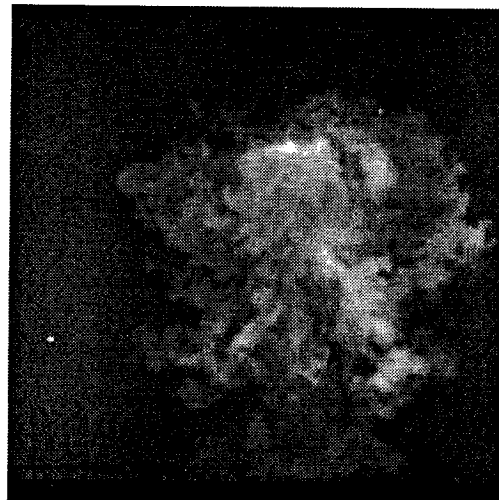
Figure 4.21. Instantaneous Rayleigh scattering images for straight case with water-seeded air fuel at twice matched pressure.

70
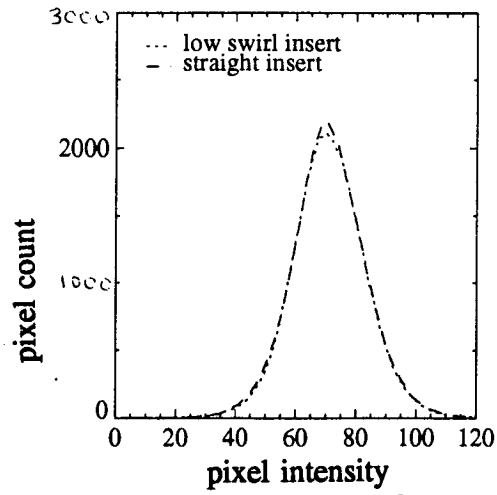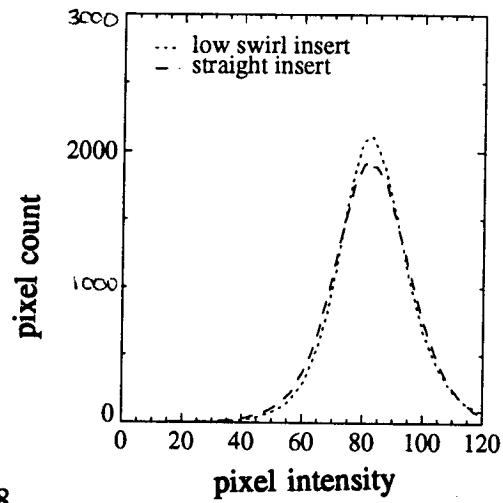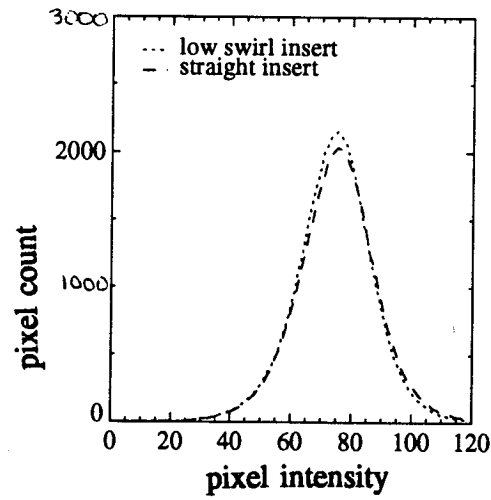
(a) $x/d_j = 7.8$

(b) $x/d_j = 15.8$

(c) $x/d_j = 23.8$

Figure 4.22. Averaged histograms of instantaneous pure Rayleigh scattering images with air fuel.
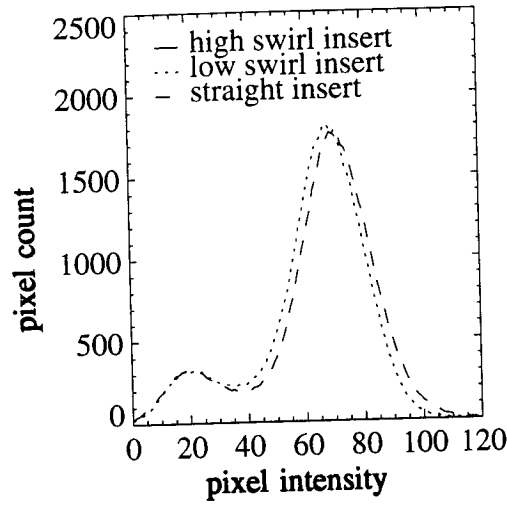
(a) $x/d_j = 7.8$
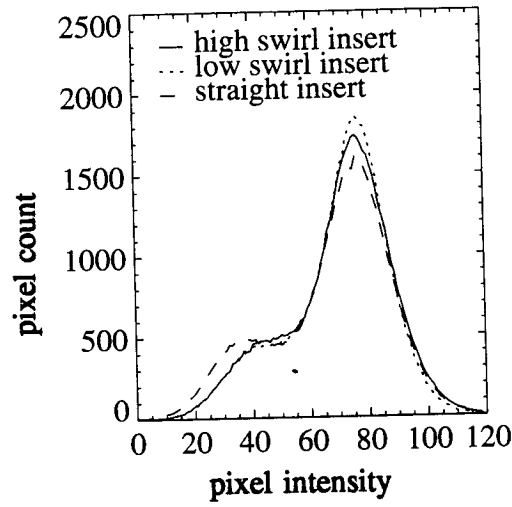
(b) $x/d_j = 15.8$
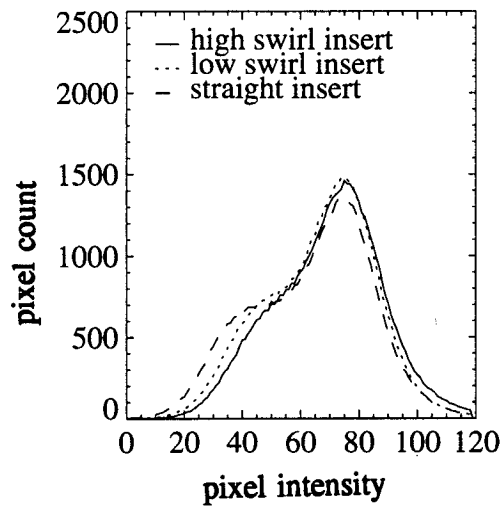
(c) $x/d_j = 23.8$

Figure 4.23. Averaged histograms of instantaneous pure Rayleigh scattering images with helium fuel.
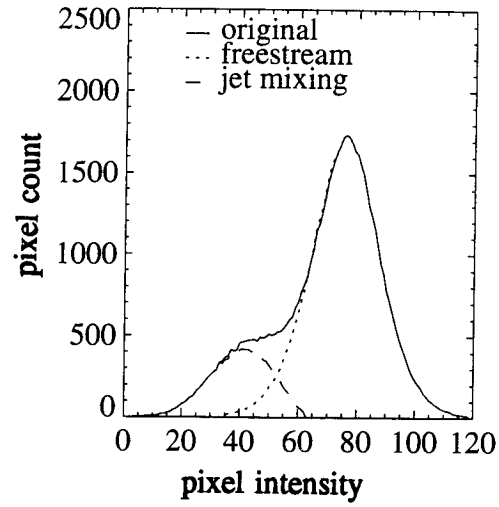
Figure 4.24. Example of method to separate freestream and jet-mixing portions of histogram.
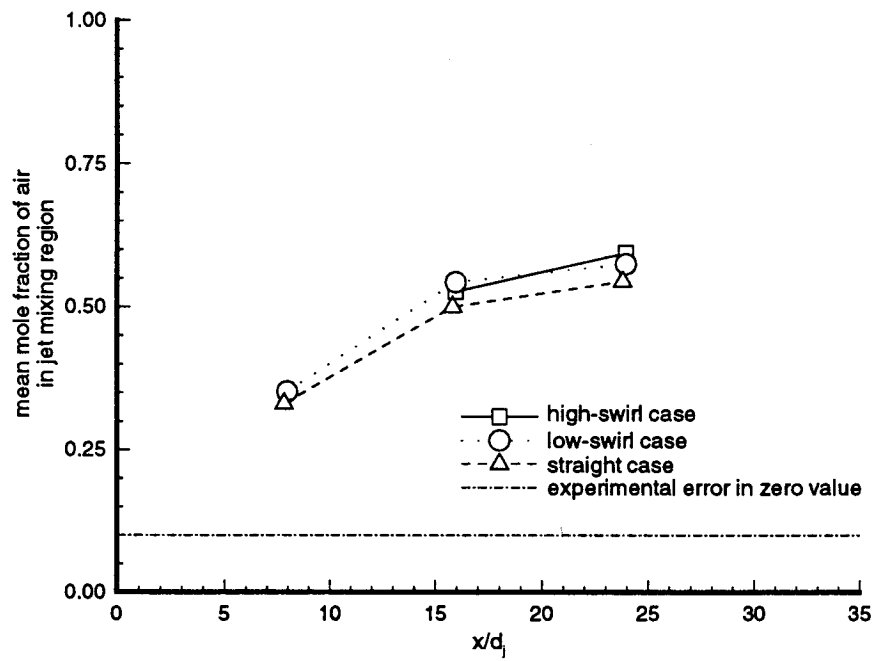
Figure 4.25. Mean mole fraction of air in jet-mixing region of flow for all three cases through duct.
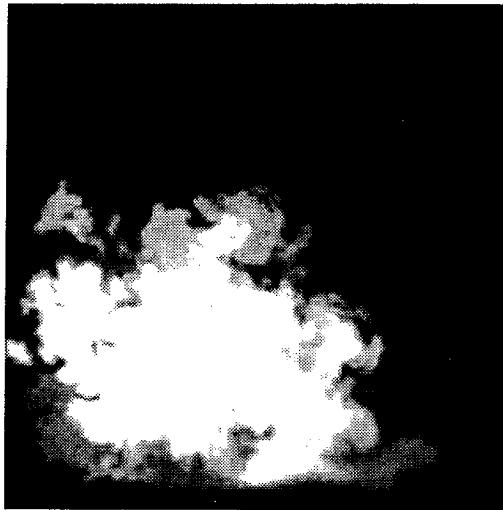
(a) original image
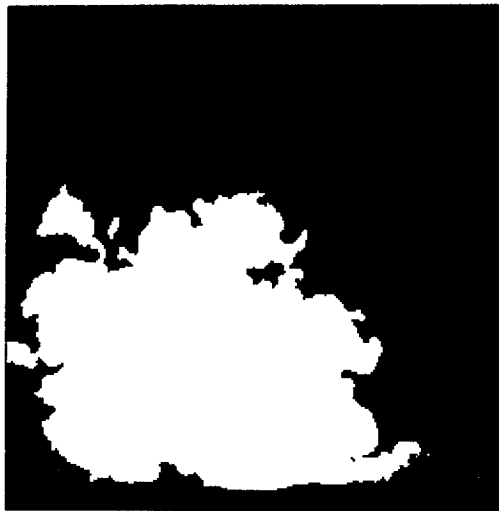
(b) thresholded image

Figure 4.26. Example of thresholding method for low-swirl case with water-seeded helium fuel at $x/d_j=23.8$.

74
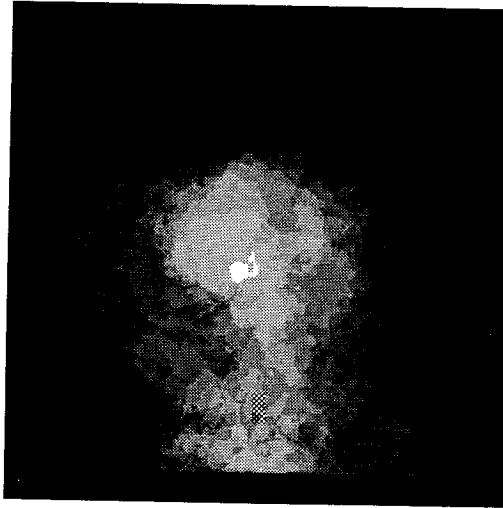
(a) straight case
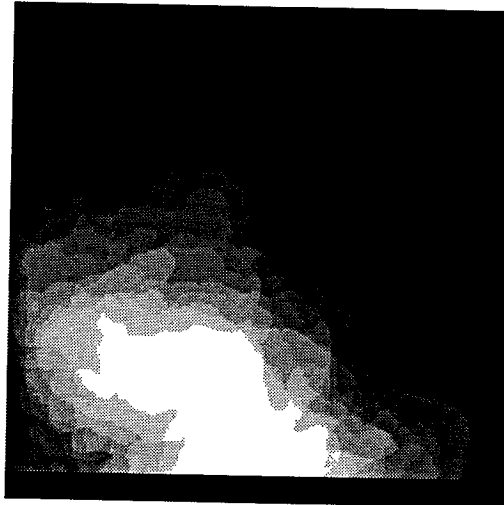
(b) low-swirl case

Figure 4.27. Averaged thresholded images of water-seeded air fuel images at $x/d_j = 23.8$.

(a) straight case
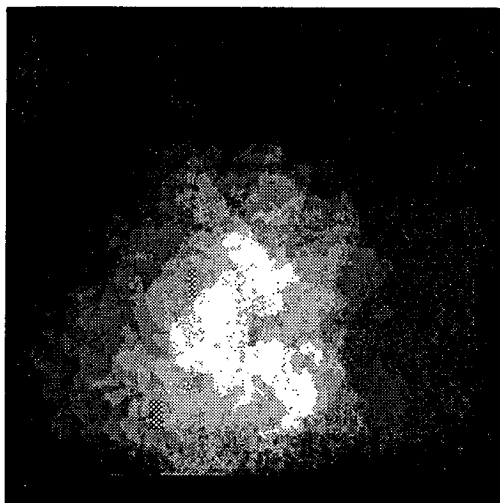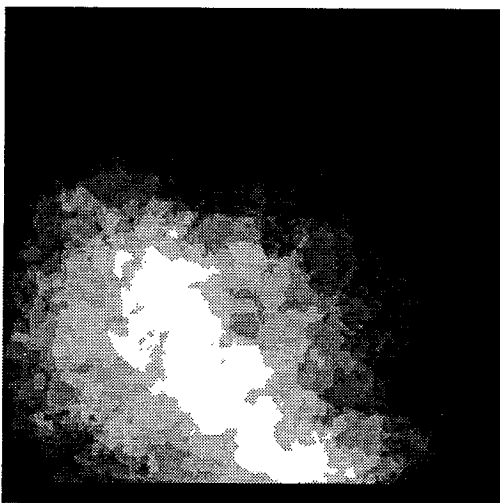
(b) low-swirl case

(c) high-swirl case
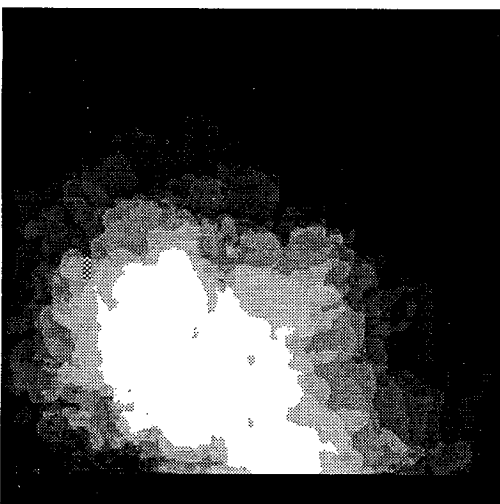
Figure 4.28. Averaged thresholded images of water-seeded helium fuel images at x/d_j=23.8.

(a) $x/d_j = 7.8$
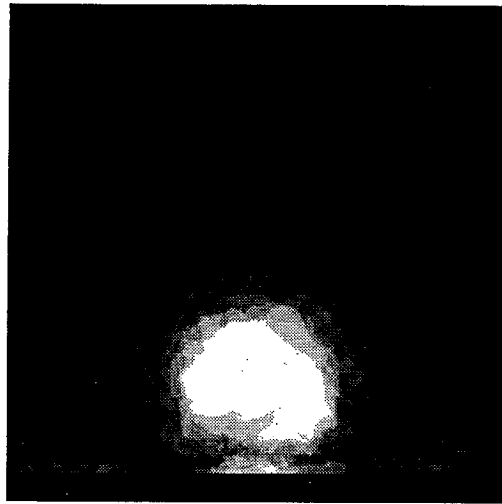
(b) $x/d_j = 15.8$
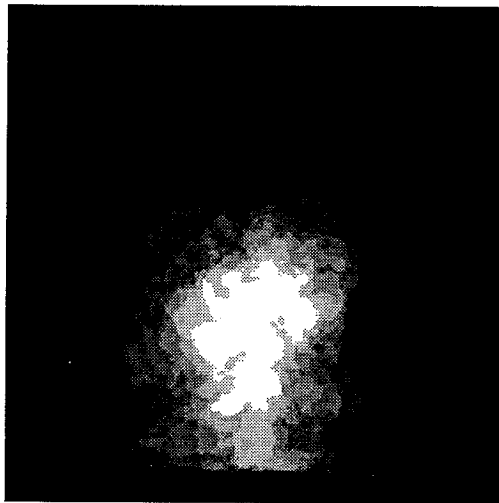
(c) $x/d_j = 23.8$

Figure 4.29. Averaged thresholded images of water-seeded air fuel images for straight case at matched pressure.

77

(a) $x/d_j = 7.8$
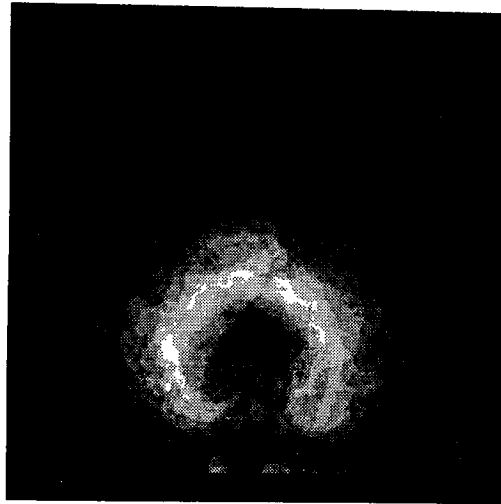
(b) $x/d_j = 15.8$
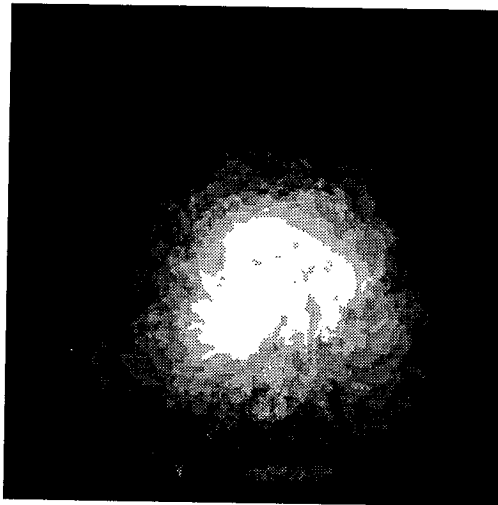
(c) $x/d_j = 23.8$
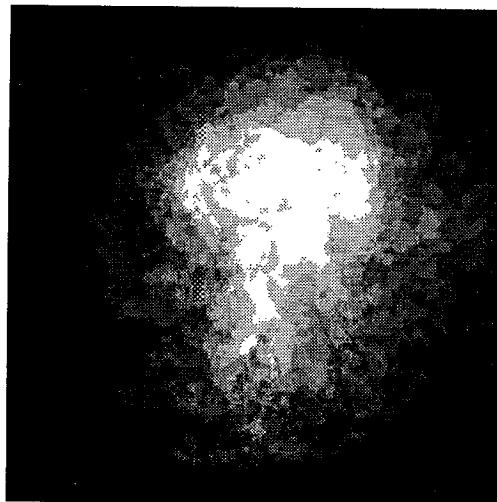
Figure 4.30. Averaged thresholded images of water-seeded air fuel images for straight case at twice matched pressure.
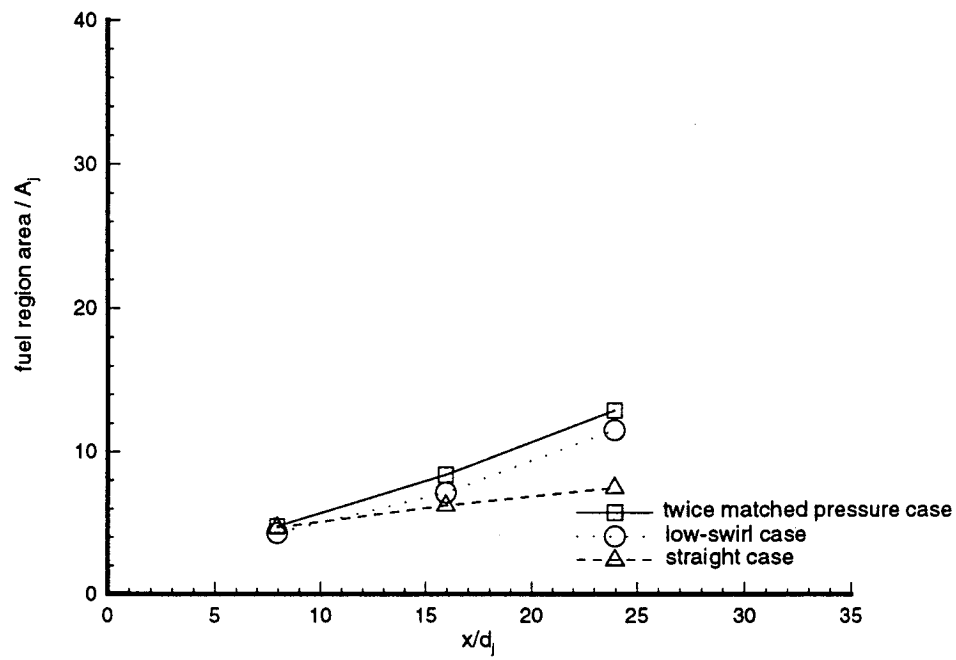
Figure 4.31. Average area of thresholded images with air fuel.
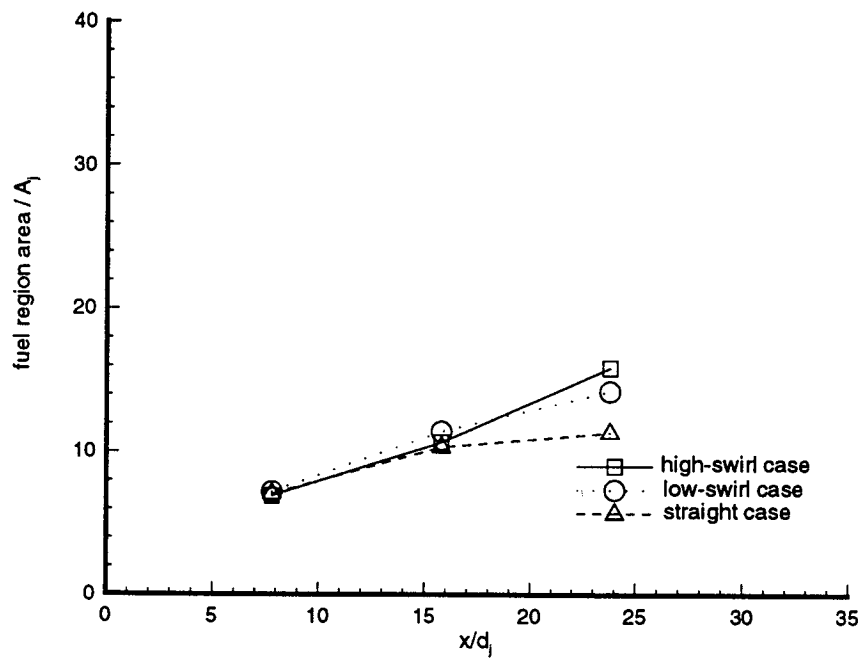
Figure 4.32. Average area of thresholded images with helium fuel.
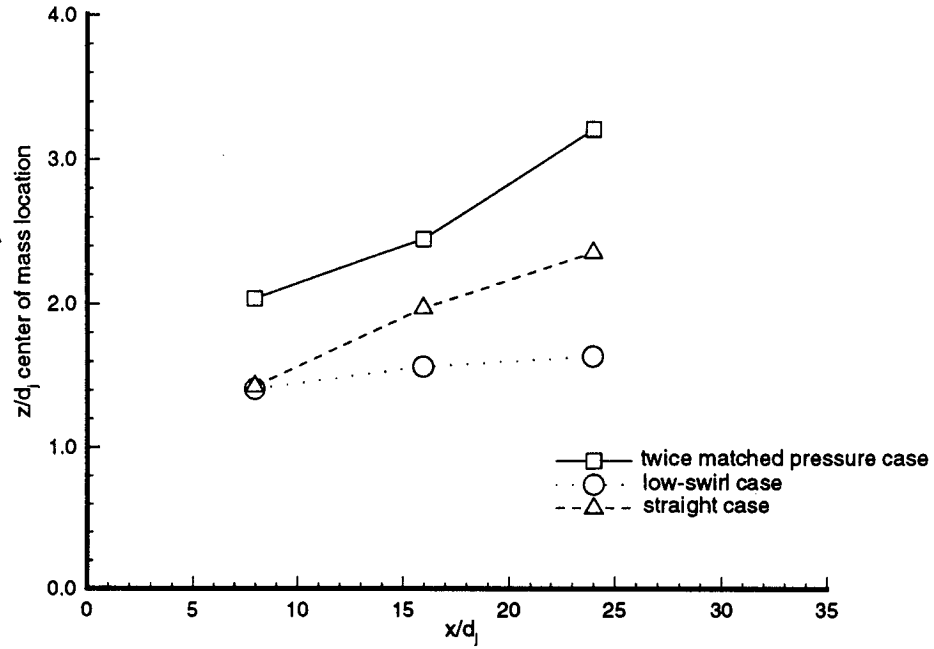
Figure 4.33. z/d_j location of center of mass of averaged thresholded image with air fuel.
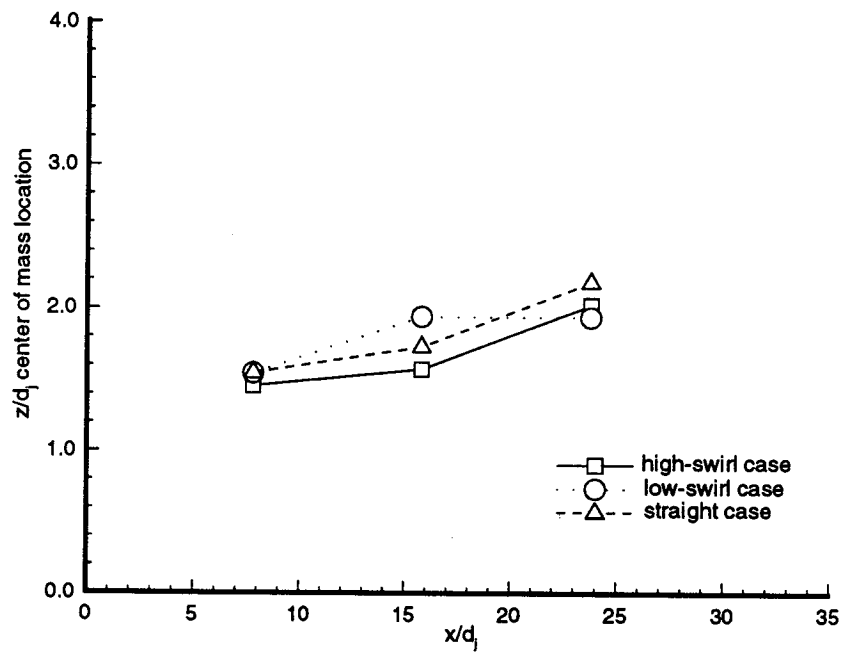
Figure 4.34. z/d_j location of center of mass of averaged thresholded image with helium fuel.

(a) straight case
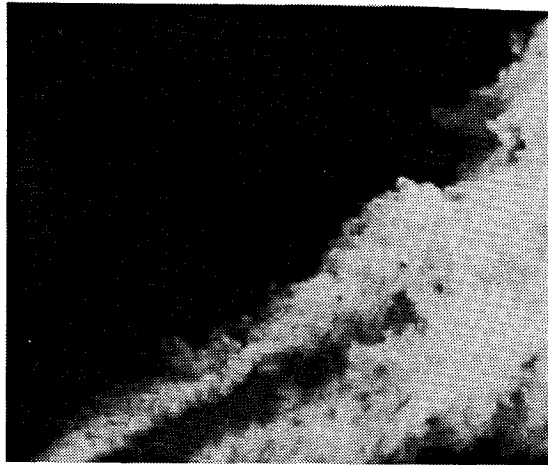
(b) low-swirl case

Figure 4.35. Instantaneous Rayleigh scattering image of fuel jet discharging into stagnant air with water-seeded air fuel at side view.
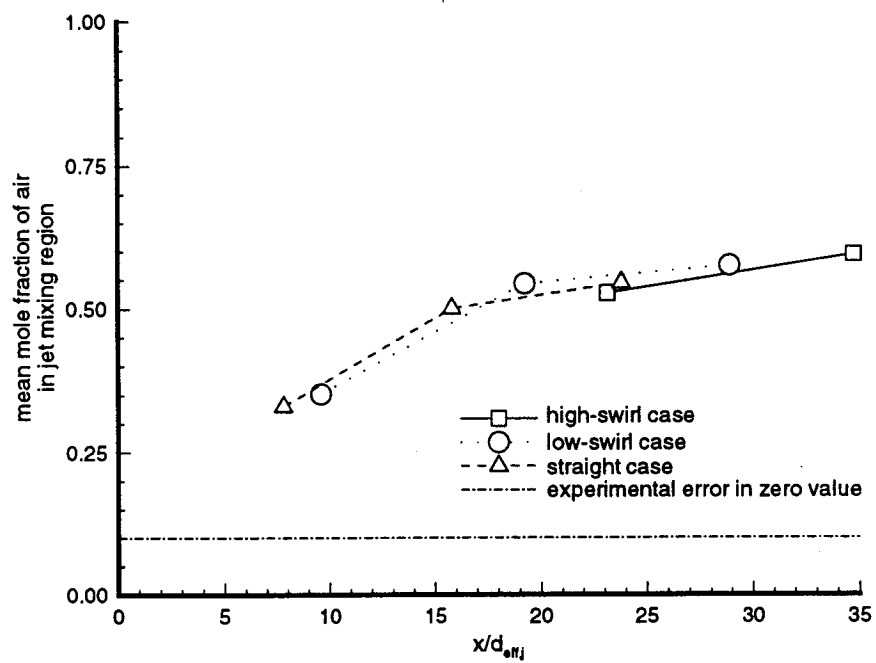
(a) straight case
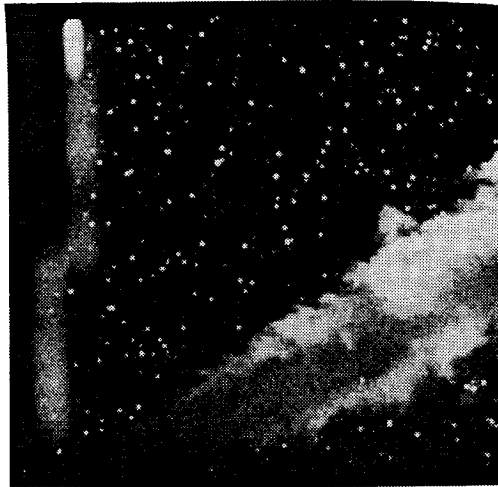
(b) low-swirl case
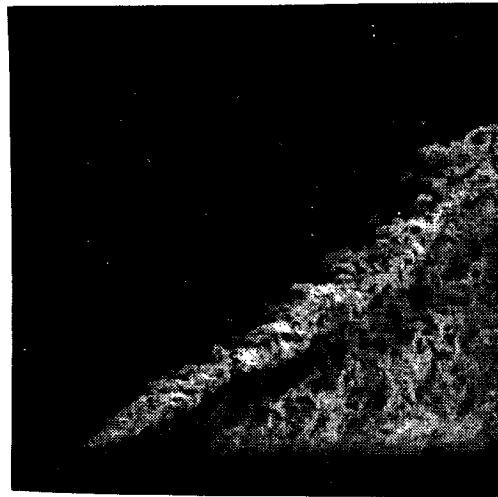
Figure 4.36. Instantaneous Rayleigh scattering image of fuel jet discharging into stagnant air with water-seeded helium fuel at side view.

Figure 4.37. Mean mole fraction of air in jet-mixing region of flow for all three cases through duct for equal mass flow rates.
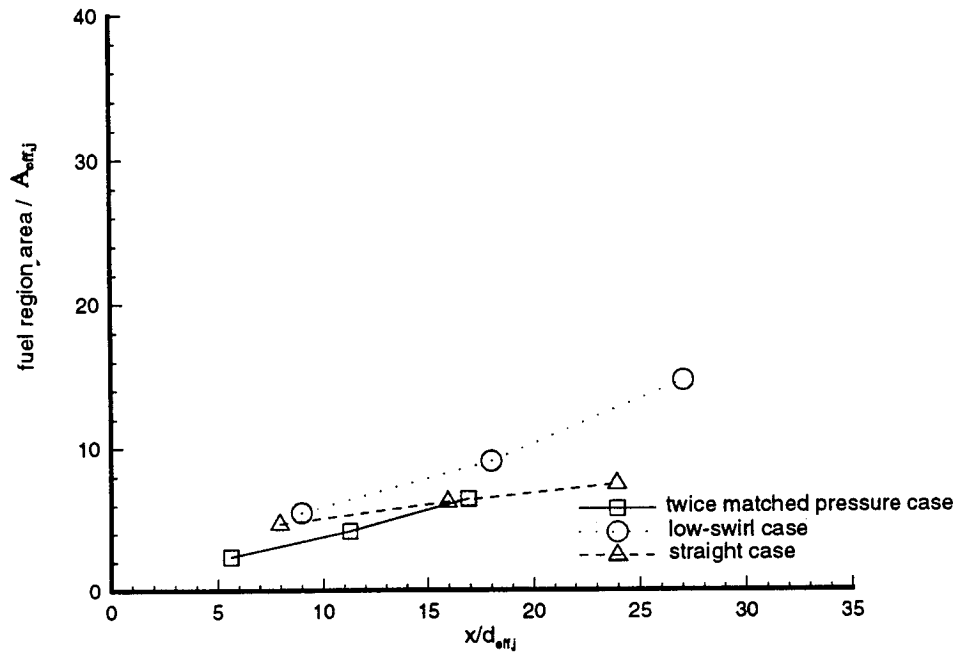
Figure 4.38. Average area of thresholded images with air fuel for equal mass flow rates.
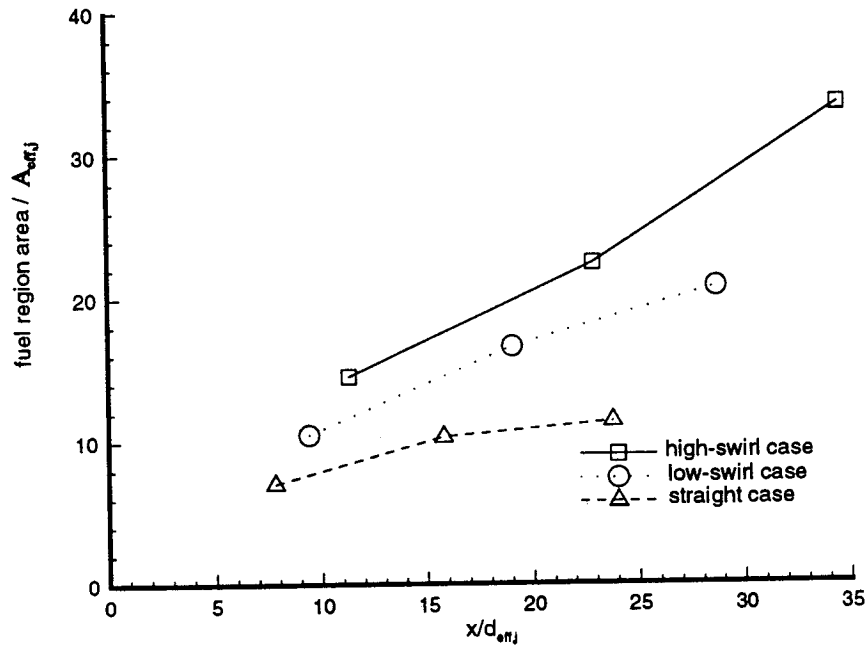

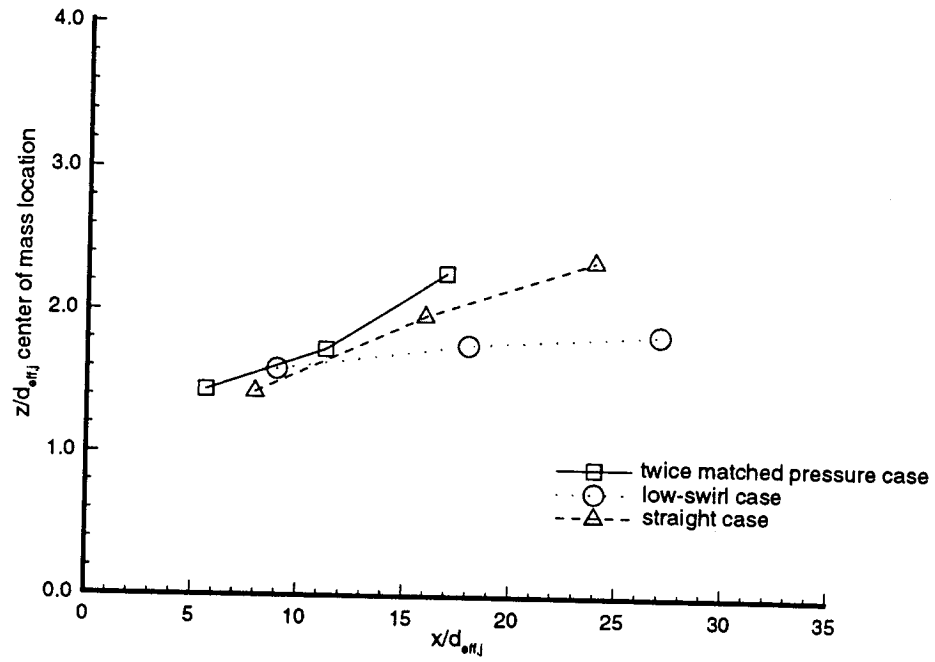Figure 4.39. Average area of thresholded images with helium fuel for equal mass flow rates.

Figure 4.40. $z/d_{eff,j}$ location of center of mass of averaged thresholded image with air fuel for equal mass flow rates.
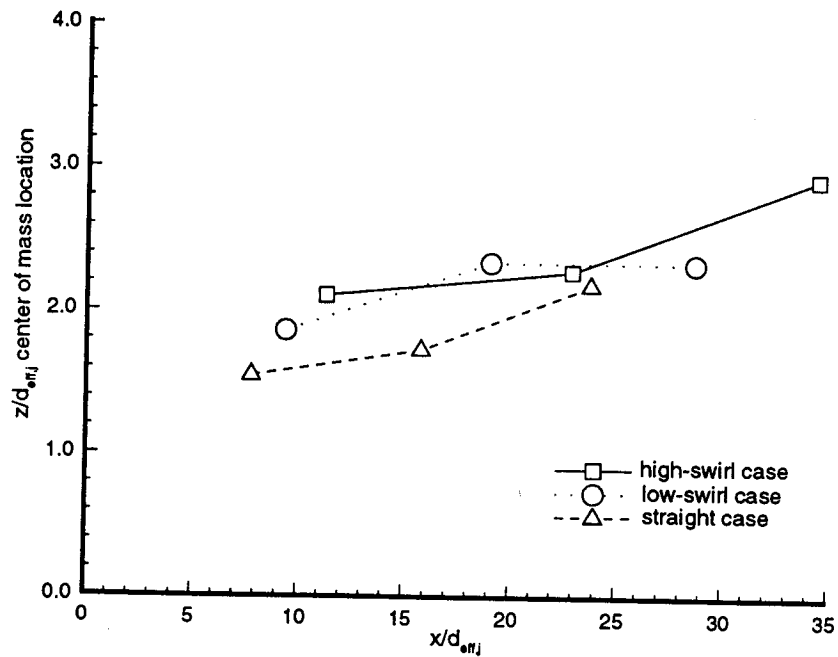

Figure 4.41. $z/d_{eff,j}$ location of center of mass of averaged thresholded image with helium fuel for equal mass flow rates.